



HAL
open science

The influence of intra-cortical microstructure on the contrast in ultrasound images of the cortex of long bones: a 2D simulation study

Amadou Sall DIA, Guillaume Renaud, Aida Hejazi Nooghabi, Quentin Grimal

► To cite this version:

Amadou Sall DIA, Guillaume Renaud, Aida Hejazi Nooghabi, Quentin Grimal. The influence of intra-cortical microstructure on the contrast in ultrasound images of the cortex of long bones: a 2D simulation study. *Ultrasonics*, 2023. hal-03781114

HAL Id: hal-03781114

<https://hal.sorbonne-universite.fr/hal-03781114>

Submitted on 20 Sep 2022

HAL is a multi-disciplinary open access archive for the deposit and dissemination of scientific research documents, whether they are published or not. The documents may come from teaching and research institutions in France or abroad, or from public or private research centers.

L'archive ouverte pluridisciplinaire **HAL**, est destinée au dépôt et à la diffusion de documents scientifiques de niveau recherche, publiés ou non, émanant des établissements d'enseignement et de recherche français ou étrangers, des laboratoires publics ou privés.

1 The influence of intra-cortical microstructure on the contrast in
2 ultrasound images of the cortex of long bones: a 2D simulation study

3 Amadou Sall DIA^{1a}, Guillaume RENAUD^{a,b}, Aida Hejazi NOOGHABI^a, Quentin GRIMAL^{2a}

^a*Sorbonne Université, INSERM, CNRS, Laboratoire d'Imagerie Biomédicale, LIB, F-75006, Paris, France*

^b*Department of Imaging Physics, Delft University of Technology, The Netherlands*

4 **Abstract**

Decreased thickness of the bone cortex due to bone loss in the course of ageing and osteoporosis is associated with reduced bone strength. Cortical thickness measurement from ultrasound images was recently demonstrated in young adults. This requires the identification of both the outer (periosteum) and inner (endosteum) surfaces of the bone cortex. However, with bone loss, the cortical porosity and the size of the vascular pores increase resulting in enhanced ultrasound scattering which may prevent the detection of the endosteum. The aim of this work was to study the influence of cortical bone microstructure variables, such as porosity and pore size, on the contrast of the endosteum in ultrasound images. We wanted to estimate the range of these variables for which ultrasound imaging of the endosteum is feasible. We generated synthetic data using a two-dimensional time-domain code to simulate the propagation of elastodynamic waves. A synthetic aperture imaging sequence with an array transducer operating at a center frequency of 2.5 MHz was used. The numerical simulations were conducted for 105 cortical microstructures obtained from high resolution X-ray computed tomography images of ex vivo bone samples with a porosity ranging from 2 to 24 %. Images were reconstructed using a delay-and-sum (DAS) algorithm with optimized f-number, correction of refraction at the periosteum, and sample-specific wave-speed. We observed a range variation of 18 dB of endosteum contrast in our data set depending on the bone microstructure. We found that as porosity increases, speckle intensity inside the bone cortex increases whereas the intensity of the signal from the endosteum decreases. Also, a microstructure with large pores (diameter > 250 μm) was associated with poor endosteum visibility, compared with a microstructure with equal porosity but a more narrow distribution of pore sizes.

These findings suggest that ultrasound imaging of the bone cortex with a probe operating at a central frequency of 2.5 MHz using refraction-corrected DAS is capable of detecting the endosteum of a cortex with moderate porosity (less than about 10%) if the largest pores remain smaller than

¹Corresponding author. E-mail address: amadou.dia@sorbonne-universite.fr

²Given by the Editor-in-Chief, Editor of this journal, Quentin GRIMAL had no involvement in the peer-review process of articles for which he was a co-author and had no access to information regarding the peer-review. Full responsibility for the peer-review process for this article was delegated to another Editor of this journal.

about 200 μm .

5 1. Introduction

6 Bone fragility associated with osteoporosis and the resulting increased risk of fracture is an
7 important medical threat as nine million fragility fractures occur annually worldwide [1]. The
8 prediction of fracture risk is based on clinical factors and, often, areal bone mineral density (aBMD)
9 measured with dual energy X-ray absorptiometry (DXA). However, many individuals who are
10 at high risk of fracture are not identified with aBMD assessed with DXA [2, 3]. Quantitative
11 ultrasound (QUS) methods to characterize trabecular and cortical bone have been developed in
12 the past three decades to overcome the limitations of DXA and provide a non ionizing, portable,
13 and affordable diagnostic tool for osteoporosis [4, 5].

14 While ultrasound imaging can accurately image the outer surface of bones [6], current clinical
15 ultrasound scanners fail to reveal their inner structure. Only recently, with adapted image recon-
16 struction methods and research ultrasound scanners, it was shown that the cortex can be imaged
17 in vivo [7, 8]. These methods have only been applied on a limited number of individuals and the
18 measurement of the cortical thickness, a key parameter for fracture risk assessment [9, 10], was
19 only shown to be feasible in young healthy adult volunteers [7].

20 Bone loss occurring as part of the natural ageing process and accelerated in osteoporosis is
21 associated with a degradation of cortical bone microstructure: unbalanced intracortical remodeling
22 leaves cavities only partially filled with newly formed bone tissue and so-called giant pores due
23 to the clustering of the remodeled cavities [11][12]. Porosity increases with age, e.g., in females
24 from about 5% at 30 years old to 15% at 80 years old [13]. This is associated with an increase
25 in pore diameter [14]. At the diaphysis of long bones, most of the cortical porosity is formed by
26 so-called Haversian canals, which are roughly cylindrical and run nearly parallel to the bone axis.
27 Previous studies have shown that the median pore diameter can vary from 40 to 200 μm between
28 individuals, for cortical bone tissue with porosity ranging from 1 to 21% [15, 16, 11, 17].

29 Ultrasound echo signals reflected at the inner surface of the cortex (endosteum) are weak
30 due to scattering by the microstructure and absorption in the viscoelastic mineralized collagen
31 extracellular matrix [18, 19]. The amplitude of the echoes backscattered from the pores may
32 be more important than that of echoes from the endosteal interface. As a consequence, a major
33 challenge for bone ultrasound imaging is to image the endosteal interface despite strong attenuation

34 and diffuse scattering by the pores. In the degraded bones of osteoporotic subjects, characterized
 35 by a higher porosity and larger pores, stronger diffuse scattering by the pores is expected compared
 36 to healthy individuals. For instance, in ultrasound images from in-vivo measurements of an ongoing
 37 study, shown in Figure 1 for illustration, the endosteal interface is found to be more visible for a
 young volunteer (26 y.o) than for an older one (61 y.o). Because little research on bone ultrasound

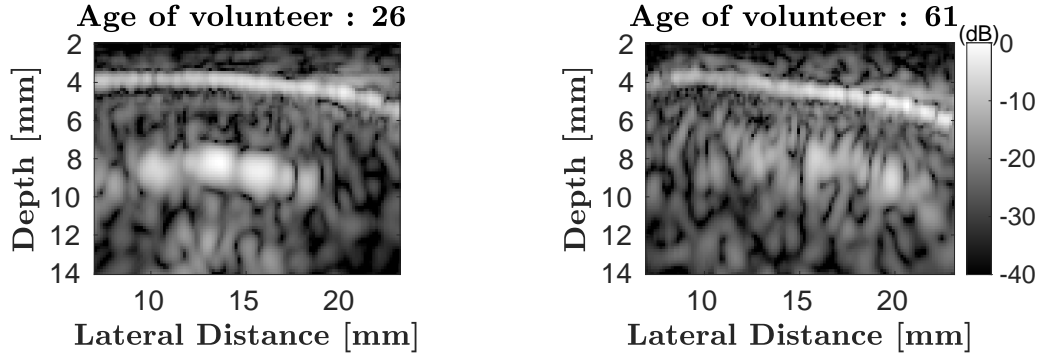


Figure 1: Illustration of degraded endosteal interface visibility with age on two subjects. Transverse ultrasound image of the tibia for two volunteers aged 26 (left) and 61 (right) are shown. The bright continuous line is the periosteal interface at a depth of about 4 mm which is perfectly visible for the two subjects. The endosteal interface at a depth of about 8 mm is more visible in the younger subject. Normalized gray scale dynamic range is given in dB. Images were obtained with a probe operating with a center ultrasound frequency of 2.5 MHz with a method similar to that described in [7].

38
 39 imaging has been conducted until now, it is yet unknown to which extent it is possible to obtain an
 40 ultrasound image of the endosteal interface of human cortical bone, in particular in osteoporotic
 41 subjects.

42 The objective of this study was to quantify the influence of cortical bone microstructure on the
 43 identification of the endosteal interface in an ultrasound image in order to estimate the range of
 44 porosity and other microstructure variables, such as pore size, for which ultrasound imaging with
 45 a conventional beamformer would be feasible. Synthetic data from two-dimensional numerical
 46 simulations using a large set of real cortical microstructures with porosity ranging from 2% to
 47 24% were generated. Images were reconstructed using a delay-and-sum algorithm with optimized
 48 f-number and correction of refraction at the bone-soft tissue interface. A similar algorithm was
 49 previously used in vivo and enabled to determine the cortical thickness of young healthy individuals
 50 [7].

51 2. Materials and Methods

52 2.1. Models of bone cortex and soft tissues

53 The two-dimensional (2D) models of bone cortex used for the simulations were generated using
54 synchrotron X-ray microcomputed tomography (SR- μ CT) three-dimensional images of human bone
55 from a previous study [20]. Briefly, samples were collected in the mid-diaphysis of the femur of 29
56 subjects (16 females and 13 males, age range: 50-95 years old). The femurs were provided by the
57 Département Universitaire d'Anatomie Rockefeller (Lyon, France) through the French program
58 on voluntary corpse donation to science. The tissue donors or their legal guardians provided
59 informed written consent to give their tissue for investigations, in accord with legal clauses stated
60 in the French Code of Public Health. For each femur, two cuboids specimens of nominal size
61 $3 \times 4 \times 5 \text{ mm}^3$ were extracted, one in the lateral and the other in the medial quadrant. Three
62 specimens which contained trabecularized cortex were discarded, resulting in a collection of 55
63 specimens for this study. SR- μ CT images of the specimens were obtained with isotropic voxel
64 size of $6.5 \text{ }\mu\text{m}$ performed on the beamline ID19 at the European Synchrotron Radiation Facility
65 (ESRF, Grenoble, France). The image processing was described previously in [21]. Briefly, the 3D
66 volume of each specimen was cropped to a perfect rectangular parallelepiped shape and slightly
67 rotated so that the geometric coordinates coincide with the material coordinates defined by the
68 faces of the specimen. Thereafter, axis 3 was approximately along the direction of osteons (and
69 diaphysis axis) and axes 1 and 2 were perpendicular to osteons. The images were then binarized
70 by single level thresholding to obtain two phases: pores and mineralized matrix with an output
71 voxel size of $10 \text{ }\mu\text{m}$, Figure 2.

72 For the 2D simulations, a set of 105 2D images were created by randomly picking slices in the
73 (1,2) plane from the 3D image stack (Figure 2) of the 55 specimens. The 2D images were sorted
74 so that their porosity (pore surface to total surface ratio) was ranging from 2% to 24%. For the
75 critical range of porosity (7 -15) % in which strong variations of the image contrast are expected,
76 we selected 5 times more slices than for low ($< 7\%$) and high ($> 15\%$) porosities.

77 Each 2D image of microstructure was used to build a model for numerical simulations: a
78 three-layer medium representing the configuration used for imaging the diaphysis of a long bone
79 with an ultrasound transducer oriented perpendicular to the bone diaphysis (Figure 3). Since
80 the original microstructure images were too small (approximately $2.7 \times 3.5 \text{ mm}^2$) to perform a
81 realistic simulation, the bone layer was created by duplicating and mirroring the microstructure of

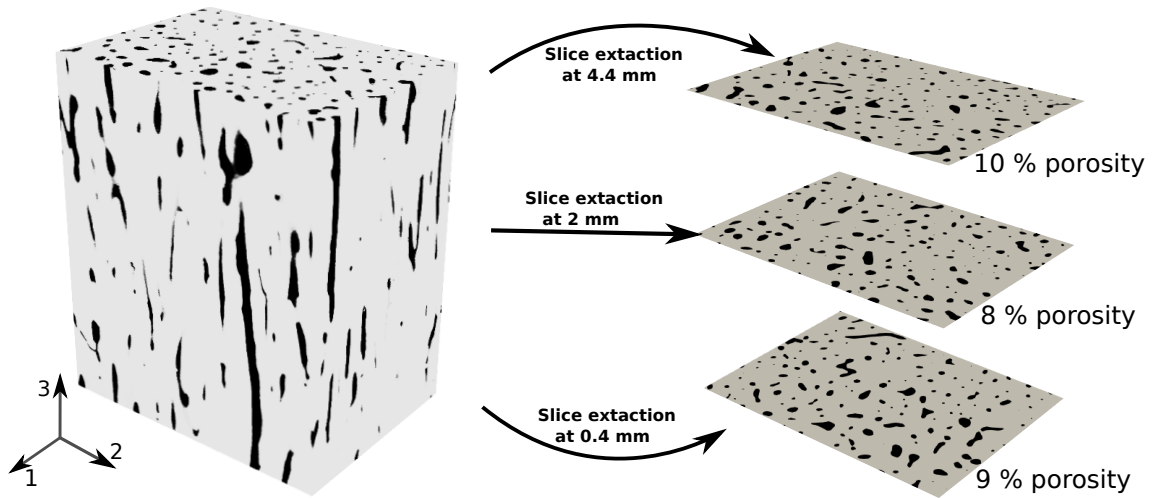


Figure 2: Binarized SR- μ CT image of a cortical bone specimen of nominal dimensions $3 \times 4 \times 5 \text{ mm}^3$ (original voxel size $6.5 \text{ }\mu\text{m}$). Black: vascular pores; light gray: mineralized matrix. Axis 1 corresponds to radial direction, axis 2 to the circumferential direction and axis 3 to the axial direction or diaphysis axis. For illustration, 3 slices extracted from the 3D volume, as used for 2D numerical simulations, are shown. 2D porosity values are given for each slice, illustrating the variable porosity in a 3D volume.

82 the original image in direction 2. A layer of soft tissue was placed above the cortical bone layer,
 83 to mimic the tissues between the probe and bone and a layer of marrow was placed below. The
 84 dimensions of the three-layer medium are given in Figure 3.

85 For the mineralized matrix of the cortical bone layer, the compressional and shear wave-speeds
 86 used in the simulation were 3496 m.s^{-1} and 1645 m.s^{-1} respectively. These values were deduced
 87 from the elastic coefficients of the bone matrix [21] (see Appendix A for details of the mass density
 88 and wave-speed estimation).

89 The material within the pores was assumed to be a fluid. The compressional wave-speed was
 90 1610 m.s^{-1} for cutaneous tissue [22] and 1410 m.s^{-1} for marrow [23]. Ultrasound attenuation in
 91 cortical bone is due to a combination of absorption by dissipative mechanisms in particular in
 92 the mineralized matrix and scattering by the pores [24]. Following the models of Yousefian et al.
 93 [18, 25], a frequency-independent absorption within the bone matrix with an absorption coefficient
 94 of 19.0 dB/cm at 2.5 MHz was modeled.

95 2.2. Pores statistics

96 The microstructure for each model was characterized by cortical porosity (Ct.Por), cortical pore
 97 density (Ct.Po.Dn in pores/ mm^2) and the distribution of pore diameters. These were calculated
 98 following the approach adopted by [26, 27]. Ct.Por was obtained by taking the ratio of the number

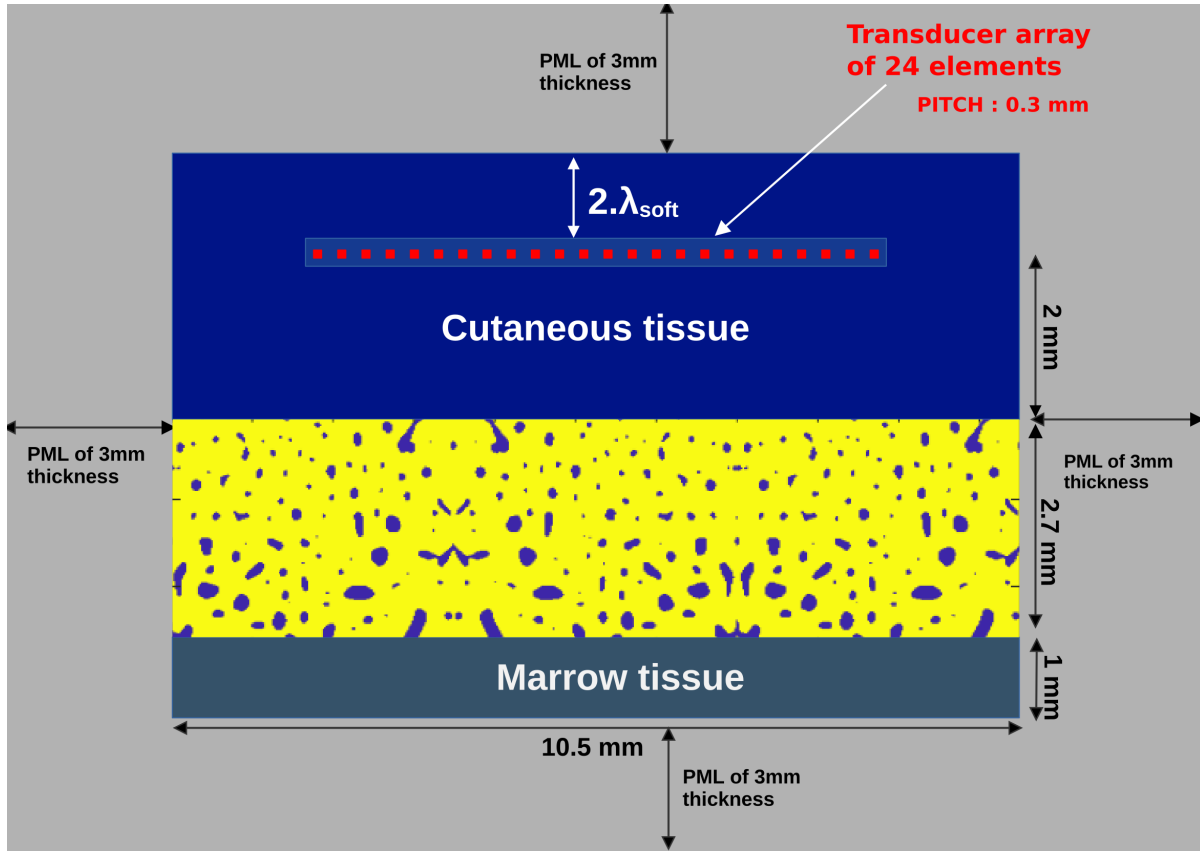


Figure 3: Three-layers model used for simulations: cutaneous tissue (blue), cortical bone tissue (yellow) and marrow tissue (bluish green) surrounded by Perfectly Matched Layers (PML, in gray).

99 of pixels associated with pores to the total number of pixels. Ct.Po.Dn was calculated as the
 100 number of pores divided by the total bone area. The diameter of each pore was calculated as the
 101 diameter of a disk of the same area. The distribution of pore diameters was characterized by the
 102 median value (Ct.Po.Dm); the 1st (Dm.DC-1) and 9th (Dm.DC-9) deciles; the average diameter
 103 of small pores (Sm.Po.Dm), i.e., of pore diameters smaller than Dm.DC-1; the average diameter
 104 of large pores (Lg.Po.Dm), i.e., of pore diameters larger than Dm.DC-9; the range of variation
 105 (Dm.Rng), i.e. the difference between the maximum and the minimum pore diameter; and the
 106 inter-decile range (Dm.IDRng).

107 In Figure 4 variations of Ct.Po.Dm and Ct.Po.Dn as a function of Ct.Por are plotted for the
 108 collection of microstructures used for the simulations.

109 2.3. Simulation of the ultrasound imaging sequence

110 We simulated the experimental configuration and acquisition sequence in [7] where an ultra-
 111 sound array is placed on the skin to image the radius or tibia in a transverse plane, that is, in a

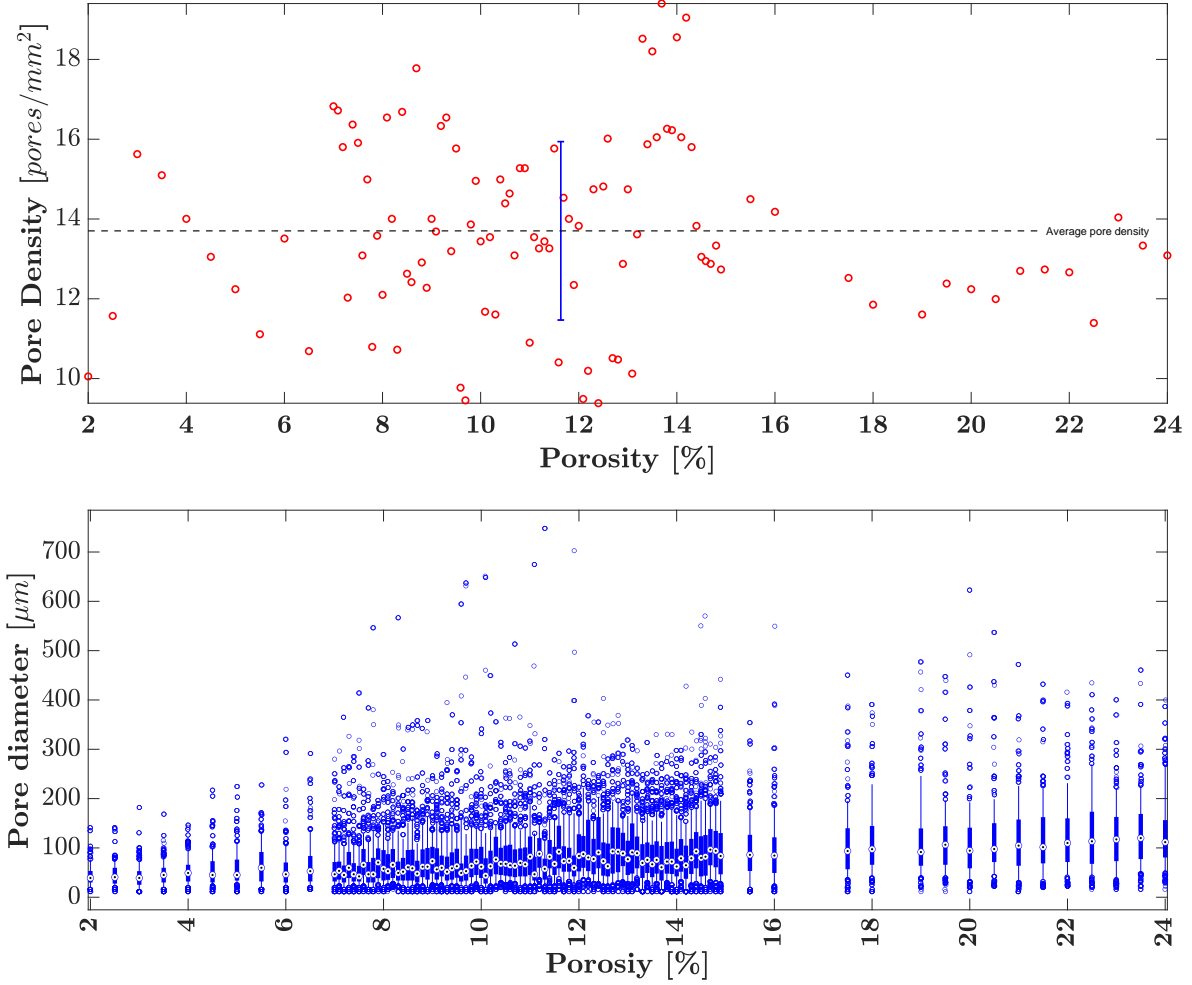


Figure 4: Pore statistics for each microstructure. Top: pore density (red circle) as a function of porosity; the black dashed line is the mean value and the standard deviation for the collection of microstructure is represented in blue. Bottom: stacked customized boxplots of pore diameter for each microstructure. Bottom and top of each box are respectively the first and last decile values, the circle in the middle of each box is the median pore diameter, the vertical line below each box extends from first decile to first quartile, the vertical line above each box extends from third quartile to ninth decile. Points below and above lines are respectively the values of diameters lower than the first decile and greater than the ninth decile

112 plane perpendicular to the diaphysis (and also perpendicular to the axis of the osteons). The sim-
 113 ulated transducer mimicks the one used in the experiment except for the number of transducers.
 114 It is a 6.9 mm array with 24 elements and a pitch of 0.3 mm (element size of 10 μm , i.e. one grid
 115 step). The transducer is placed in the upper layer at a depth of 2 wavelengths to avoid border
 116 effects, and centered horizontally (Figure 3).

117 An acquisition scheme for synthetic aperture imaging was simulated: each individual element in
 118 the array successively transmitted a Gaussian-windowed tone burst with a central frequency of 2.5

119 MHz (3dB bandwidth= 1.33 MHz, see Figure 5). For each transmission, the backscattered signals
 120 were recorded by all the elements of the array. Therefore, for each bone microstructure, 24×24
 backscattered synthetic signals were recorded.

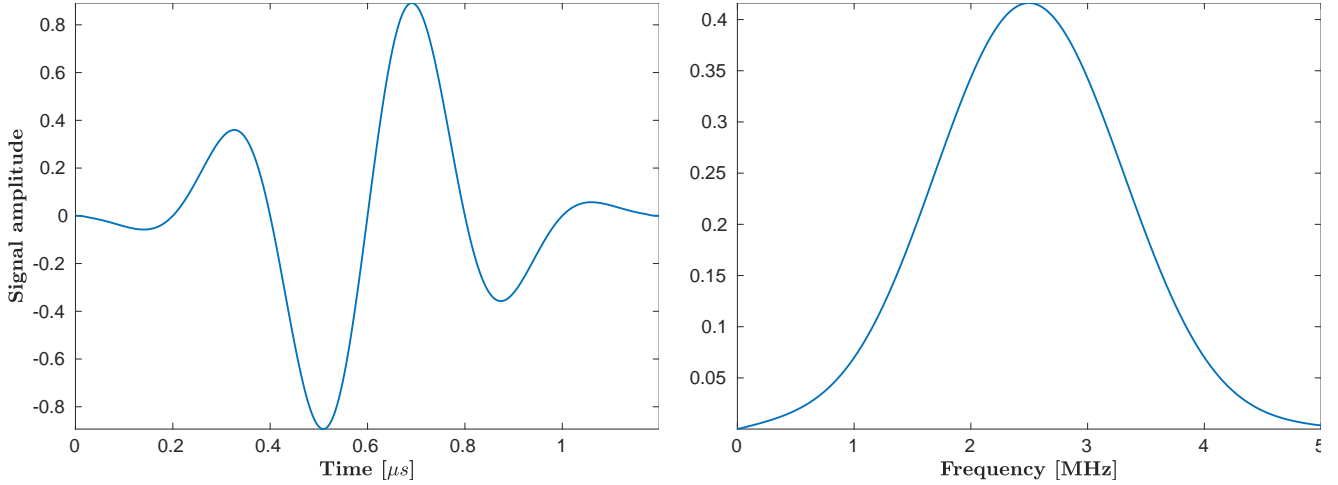


Figure 5: Emitted tone burst in temporal domain (left) and in frequency domain (right).

121
 122 Elastic wave propagation in the three-layer medium was simulated with the Finite Difference
 123 Time-Domain (FDTD) open-source code SimSonic [28, 29]. To avoid reflections on the boundaries
 124 of the simulation domain, a Perfectly Matched Layer (PML) boundary condition (3 mm thickness,
 125 approximately 5 wavelengths in soft tissues) was set (Figure 3). The spatial grid size Δx for the
 126 FDTD simulation was equal to the microstructure image pixel size (10 μm). This leads to a mesh
 127 size equivalent to 56 points per wavelength in marrow at the center frequency, which is sufficient
 128 to model accurately the wave propagation with reasonably small numerical dispersion [30]. The
 129 simulation time step was chosen with respect to the Courant–Friedrichs–Lewy (CFL) stability
 130 conditions for 2D simulations. A constant value of $CFL = 0.99$ was used for these simulations.

131 2.4. Cortical bone wave-speed estimation

132 The ultrasound wave-speed in the bone layer (Figure 3) must be known to perform the refraction
 133 corrected image reconstruction as proposed in [7]. It is a priori unknown as it depends on the
 134 specific microstructure considered. Note that the combination of the isotropic elastic properties
 135 for the bone matrix with the quasi-random distribution of the pores in the plane (1, 2), leads to
 136 isotropic properties in this plane at the scale of the wavelength, which is also the millimeter scale
 137 or mesoscale [31]. Additional simulations were performed in order to estimate this wave-speed.
 138 A plane wave at normal incidence was emitted by the array using the signal shown in Figure 5.

139 Virtual receivers were placed inside bone along 5 equally spaced lines (spacing=0.5 mm) parallel
 140 to periosteal and endosteal interfaces. The waveforms recorded on each line of receivers were
 141 coherently summed and the time-of-flight was estimated from the first received signal peak. The
 142 wave-speed in the cortical bone is finally obtained by linear regression of time-of-flights measured
 143 at the 5 different depths (see Figure B.13 in Appendix B). As an alternative method, the wave-
 144 speed could be obtained by finding within a range of values, the wave-speed that maximizes the
 145 focus quality at the endosteal interface as it was done in in-vivo [7].

146 2.5. Image reconstruction with a refraction-corrected delay-and-sum algorithm

147 Delay-and-sum (DAS) algorithm with a constant f-number in receive throughout the image is
 148 used for image reconstruction [32]. DAS was chosen as it is the most extensively used beamforming
 149 algorithm, and also because it was used for the first in-vivo imaging of the bone cortex in [7]. A
 150 hanning window was applied to the receiver sub-aperture. A preliminary study aimed to determine
 151 the optimal f-number that maximizes the image contrast for the detection of the endosteal interface,
 152 the optimal f-number was 1.9 (see Appendix C). This way, DAS is used at its highest potentiality
 153 as described by [32]. The synthetic aperture sequence led to 24 low resolution images which were
 154 coherently summed to get a high contrast image. The delays used in the DAS algorithm account
 155 for refraction at all the interfaces. The implementation described in [7] was used to calculate
 156 the delays: for each array element and image pixel, Fermat's principle is used to calculate the
 157 travel time through the multi-layered medium. Only the contribution of longitudinal waves were
 158 considered, i.e. the arrival times of wave contributions associated with the shear waves were
 159 disregarded. The ultrasound longitudinal wave-speed used for the bone layer was different for each
 160 microstructure as explained in section 2.4.

161 2.6. Endosteal interface visibility quantification

To evaluate image quality, i.e., the visibility of interfaces, the relative interface contrast (C_{EP})
 and the endosteal interface contrast (C_{EI}) were defined as follows:

$$C_{EP} = \frac{\mu_E}{\mu_P} ; C_{EI} = \frac{\mu_E}{\mu_I},$$

162 where μ_I , μ_E and μ_P are respectively the average image intensities in the center of the cortex, at
 163 the endosteal and periosteal interfaces. The regions of interest (ROI) used for the calculation of
 164 μ_I , μ_E and μ_P , are defined in Figure 6 where the red box represents the inner bone ROI, the yellow

165 and blue boxes represent respectively the periosteal interface ROI and the endosteal interface ROI.
 166 Each ROI had a height of 0.8 mm and a width of 6.5 mm.

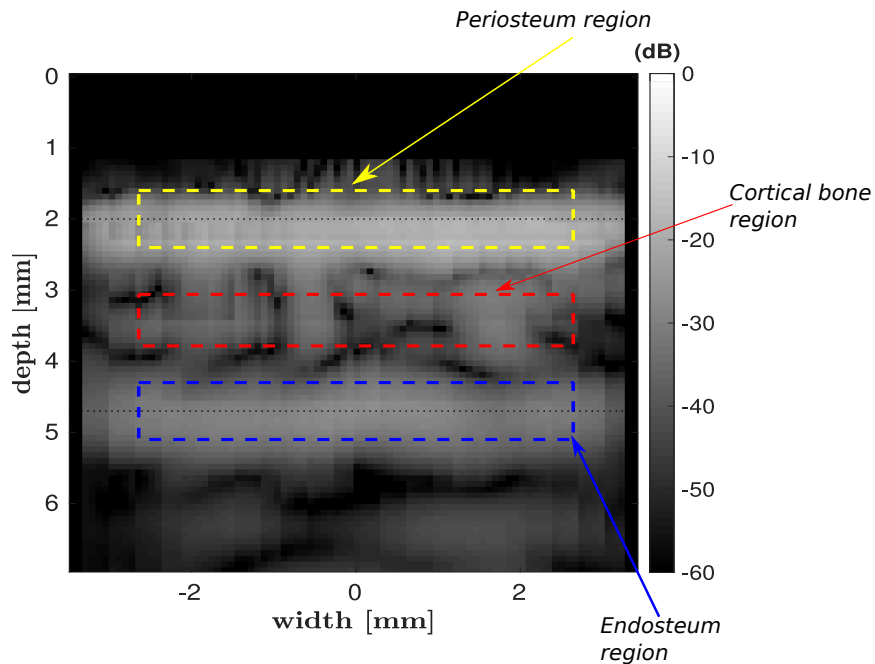


Figure 6: A typical reconstructed image for the simulation configuration shown in Figure 3. The yellow, red and blue ROIs were used to evaluate periosteum, inner bone, and endosteum contrasts, respectively.

167 Because the amplitude of the reflection at the periosteal interface is only slightly influenced
 168 by the porosity, C_{EP} variations reflect the variations of the absolute visibility of the endosteal
 169 interface. C_{EI} evaluates how well the endosteal interface can be distinguished from the speckle
 170 inside the bone. On decibel scale, a positive value of C_{EI} means that endosteal interface is clearly
 171 visible while a negative value means that the endosteal interface is poorly visible.

172 2.7. Data Analysis

173 A correlation analysis was conducted to identify the microstructure parameters defined in 2.2
 174 of most important influence on endosteal interface visibility metrics (C_{EI} and C_{EP}). Normality
 175 of the distribution of the variables was evaluated using the Shapiro-Wilk test and we found that
 176 most of the variables were not normally distributed. Therefore, Spearman rank coefficients were
 177 used.

178 Correlations were considered statistically significant for $p < 0.05$. Statistical analyses were
 179 made using the Matlab 2018b Statistics Toolbox (Mathworks Inc., Natick, MA, USA). The pat-

180 terns of variation of C_{EI} and C_{EP} with the three most important microstructure parameters were
 181 investigated. The purpose was to assess the range of values of the microstructure parameters, in
 182 particular porosity, for which the endosteal interface is visible.

183 Finally, the collection of images from all microstructure are analyzed and characteristic images
 184 to best illustrate the effect of the microstructure parameters on the appearance of the endosteal
 185 surface in the images were selected.

186 3. Results

187 3.1. Wave-speed in cortical bone models

188 Figure 7 shows the wave-speed in cortical bone estimated for each microstructure as a function
 189 of Ct.Por . Wave-speed varied from about 2900 to 3400 $m.s^{-1}$ as cortical porosity decreased from
 190 24 to 2 %, that is a variation of wave-speed of about 16%.

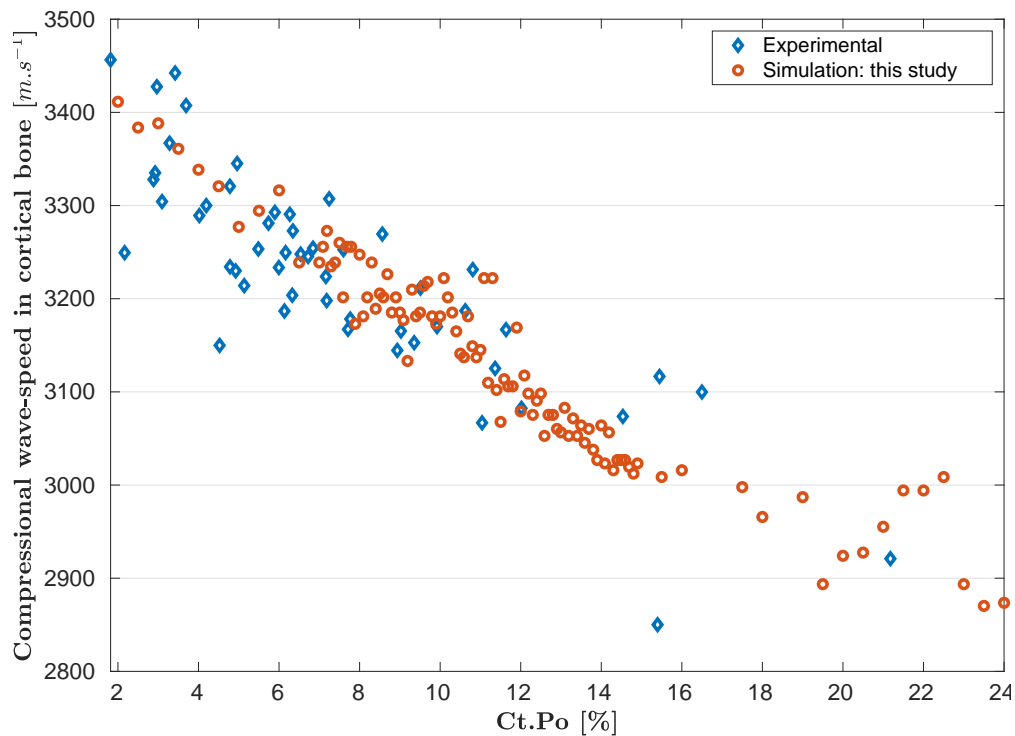


Figure 7: Simulated (red circles) and experimental (blue diamonds) wave-speed against porosity (Ct.Por).

191 For comparison, experimental values that were deduced from experimental elastic coefficients
 192 obtained by Cai et al. [33] on the same collection of bone specimens (see in Appendix B the details
 193 on experimental wave-speed determination) are also shown. Linear regression models between
 194 wave-speed and Ct.Por for both experimental ($V_1^{exp} = 3404.5 - 23.83 \times Ct.Por$, $RMSE =$

195 61.9 m.s⁻¹) and synthetic data ($V_1^{sim} = 3406.5 - 23.73 \times Ct.Por$, $RMSE = 37.8$ m.s⁻¹) had
 196 very close parameters and were in accordance with literature [34].

197 3.2. Descriptive statistics

198 The values of microstructural properties, wave-speed in cortical bone and interface visibility
 metrics are summarized in Table 1

	Median	QT-1	QT-3	MIN	MAX
Ct.Por [μm]	11.19	8.57	13.83	2.00	24.00
Ct.Po.Dm. [μm]	67.70	57.26	84.81	39.09	119.95
Ct.Po.Dn. [pores/ mm^2]	13.51	12.27	15.27	9.38	19.40
Dm.DC-1 [μm]	25.23	22.57	31.92	15.96	52.93
Dm.DC-9 [μm]	155.98	133.51	186.05	73.99	271.05
Lg.Po.Dm [μm]	213.01	186.06	238.79	97.95	337.39
Sm.Po.Dm [μm]	18.20	15.27	22.53	11.28	38.42
Dm.Rng [μm]	323.45	273.90	392.15	129.65	736.69
Dm.IDRng [μm]	132.62	106.56	154.74	54.04	229.13
V_1^{sim} [m.s ⁻¹]	3137.13	3050.90	3210.75	2870.30	3411.42
C_{EI} [dB]	0.86	-0.59	3.33	-8.31	18.57
C_{EP} [dB]	-6.81	-8.15	-5.20	-11.35	-1.89

Table 1: The median, minimum value (MIN), maximum value (MAX), first (QT-1) and last (QT-3) quartile of the visibility metrics (C_{EI} , C_{EP}), the wave-speed in cortical bone and the pore microstructural variables (defined in section 2.2)

199

200 3.3. Influence of microstructure on image contrasts

201 Spearman rank correlation coefficients between image quality metrics (C_{EI} , C_{EP}) and pore
 202 characteristics are given in Table 2. Ct.Po.Dn was not significantly correlated to the interface
 203 metrics, therefore it was discarded for the rest of the analysis. Negative correlations were found
 204 for the rest of the variables. Among all variables, the strongest correlation coefficients were for
 205 Lg.Po.Dm, Ct.Por, Dm.IDRng, and Dm.DC-9 (r_s from -0.61 to -0.71, $p < 0.001$). Correlation for
 206 Dm.Rng and Ct.Po.Dm were moderate (r_s from -0.48 to -0.52, $p < 0.001$). Smaller correlations
 207 for Dm.DC-1 and Sm.Po.Dm (r_s from -0.23 to -0.33, $0.001 < p < 0.05$) were found.

Pore characteristics	C_{EI}	C_{EP}
Lg.Po.Dm	-0.71^2	-0.67^2
Ct.Por	-0.66^2	-0.63^2
Dm.IDRng	-0.65^2	-0.61^2
Dm.DC-9	-0.62^2	-0.59^2
Dm.Rng	-0.52^2	-0.48^2
Ct.Po.Dm	-0.50^2	-0.48^2
Dm.DC-1	-0.33^1	-0.29^1
Sm.Po.Dm	-0.27^1	-0.23^1
Ct.Po.Dn	$0.08^{n.s}$	$0.11^{n.s}$

Table 2: Spearman correlation coefficient r_s between image quality metrics and microstructural properties. C_{EI} : endosteal-interface contrast, C_{EP} : relative interface contrast. $n.s$: not significant $p > 0.05$, 1 : $0.001 < p < 0.05$, 2 : $p < 0.001$

208 In figure 8, the variations of averaged pixel intensity in the three ROIs, C_{EI} and C_{EP} are
209 shown for all microstructures as function of Lg.Po.Dm, Ct.Por, and Dm.IDRng which were found
210 to be the most important variables (Table 2). Each point corresponds to a specific microstructure.
211 First, we observe the relatively small variations of the periosteum mean intensity (blue curve)
212 with respect to microstructure parameters. As a consequence, C_{EP} essentially evaluates endosteal
213 interface contrast. As expected, this value is always negative because the endosteal surface is less
214 visible than the periosteal surface.

215 Second, endosteal interface mean intensity (red curve) decreases while that of the internal
216 bone speckle intensity (orange curve) increases for increasing values of microstructure parameters
217 reflecting the degradation of bone microstructure. C_{EI} , which is by construction our metric best
218 reflecting the visibility of the interface, varies between about -5 dB and 15 dB. Negative values
219 correspond to speckle intensity inside bone larger than endosteal interface intensity. For small
220 "large pore" size (Lg.Po.Dm $< 200 \mu\text{m}$), low cortical porosity (Ct.Por $< 10\%$) and weak pore
221 size dispersion (Dm.IDRng $< 100 \mu\text{m}$), C_{EI} is positive for most of the microstructures while it is
222 negative for large "large pore" size (Lg.Po.Dm $> 250 \mu\text{m}$), high cortical porosity (Ct.Por $> 15\%$)
223 and strong pore size dispersion (Dm.IDRng $> 170 \mu\text{m}$). For intermediate values, C_{EI} hovers
224 around 0 dB.

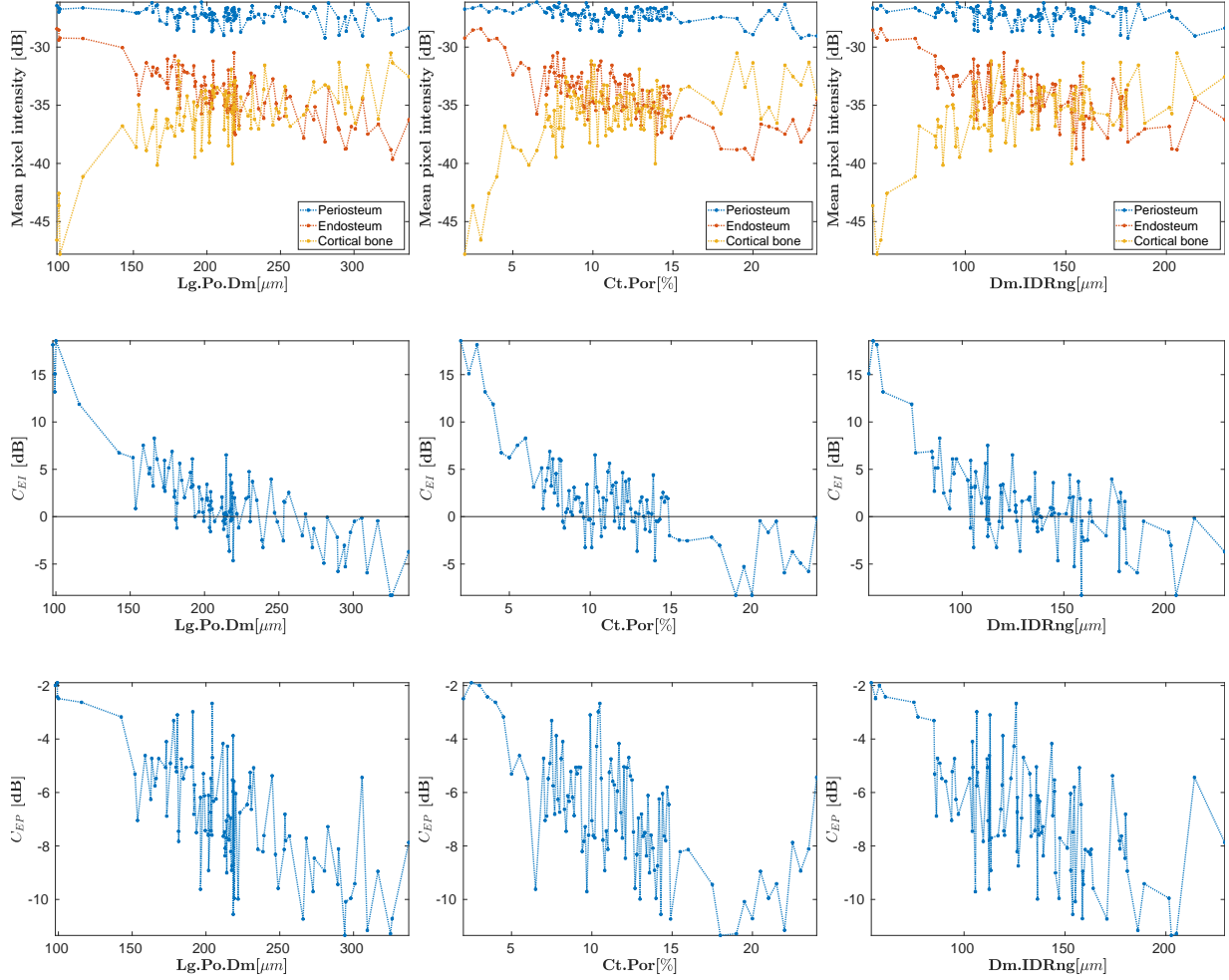


Figure 8: Average pixel intensity for the three ROIs (top), bone-endosteum contrast C_{EI} (middle) and interface contrast C_{EP} (bottom). The evolution of these variables for "large pores" size (Lg.Po.Dm), porosity (Ct.Por), and pore diameter dispersion (Dm.IDRng) are shown.

225 The reconstructed images for all microstructures are provided in the supplementary material.
 226 In the following, a set of representative images are presented. Figure 9 shows a selection of images
 227 for different porosity values. Lg.Po.Dm and C_{EI} are given for each image. The periosteal interface
 228 is clearly visible as a bright zone centered at 2 mm-depth. The endosteal interface at 4.7 mm-depth
 229 is more or less visible depending on the microstructure. With increasing porosity, speckle intensity
 230 inside bone increases and endosteal interface visibility fades. On these images, for porosities of
 231 2, 5, and 8% the endosteal interface stands out from inner cortical bone speckle and C_{EI} values are
 232 positive. For porosities of 13, 16 and 20 %, speckle intensity inside the bone becomes dominant,
 233 the endosteal interface can hardly be distinguished, and C_{EI} values are negative.

234 As Lg.Po.Dm was found to be relatively strongly correlated to the image contrast, Figure 10

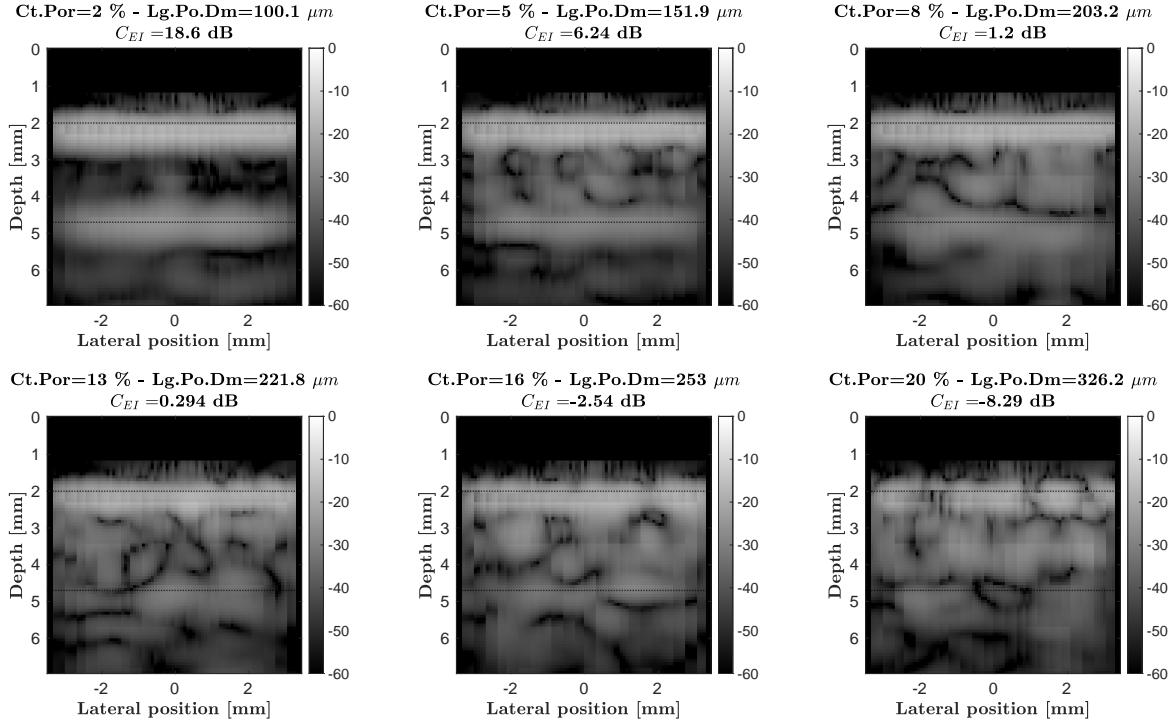


Figure 9: Reconstructed ultrasound images from simulated data for six microstructures for increasing porosities. 1st row (from left to right): 2, 5 and 8 % porosity, 2nd row: 13, 16 and 20% porosity. Lg.Po.Dm and C_{EI} are given for each image. The black dotted lines represent the true positions of the periosteal and endosteal interfaces. Each image is reconstructed using DAS with an optimized receive f-number of 1.9. The intensity is log-compressed and displayed with a dynamic range of 60 dB.

235 shows reconstructed images for microstructures with a similar porosity around 10.5% ($\pm 1\%$), and
 236 with increasing Lg.Po.Dm spanning the range 183–272 μm . For these microstructures, C_{EI} values
 237 decreased from 5.63 dB to -3.25 dB. Endosteal interface is visible for images on the first row whilst
 238 it is not for the images on the second row. As an example, figure 10 shows that the endosteal
 239 interface is perfectly detectable ($C_{EI} = 5.63$ dB) for 11.19 % porosity and Lg.Po.Dm= 183.3 μm
 240 and not visible ($C_{EI} = -3.25$ dB) for 10.09 % porosity and Lg.Po.Dm= 239.3 μm , illustrating a
 241 strong influence of the diameter of large pores on the image contrasts.

242 4. Discussion

243 4.1. Impact of the intra-cortical microstructure on image contrast

244 In this study, the effect of cortical bone microstructure on the quality of ultrasound images
 245 of the cortex is investigated. The contrast should be sufficient to allow the identification of the
 246 endosteal interface in order to assess cortical thickness, an important biomarker of bone health

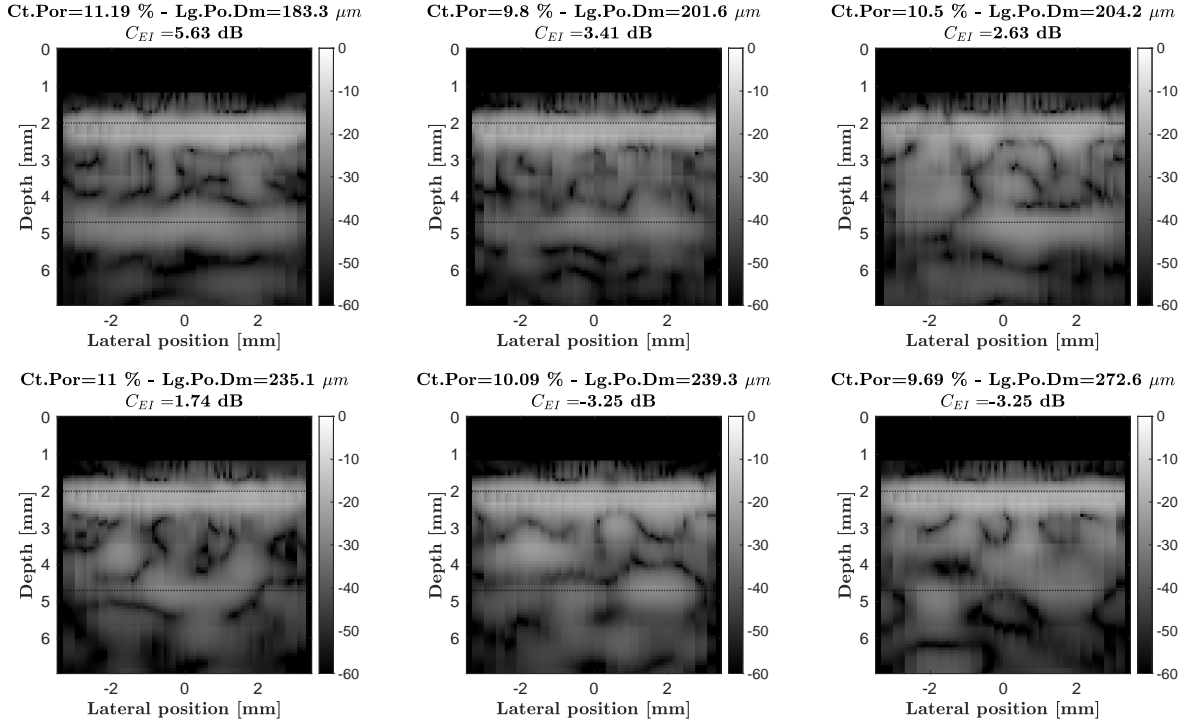


Figure 10: Reconstructed ultrasound images from simulated data for six microstructures with nearly equal porosity (around 10.5%) but increasing "large pore" size (Lg.Po.Dm). Ct.Por and C_{EI} are given for each image. The black dotted lines represent the true positions of the periosteal and endosteal interfaces. Each image is reconstructed using DAS with an optimized receive f-number of 1.9. The intensity is log-compressed and displayed with a dynamic range of 60 dB.

247 [5, 35]. Numerical simulations with a collection of 105 high-resolution images of microstructure
 248 (porosity ranging from 2 to 24%) were used in order to cover the diversity of porosity, pore size
 249 and pore distribution met in human cortical bone. Indeed, with ageing and osteoporosis, cortical
 250 bone porosity and pore size increases. This degradation of the microstructure is challenging for
 251 ultrasound imaging.

252 The simulation framework was validated based on the excellent agreement found between ex-
 253 perimental wave-speed values and those recovered from numerical simulations (Figure 7 and Ap-
 254 pendix B). Image reconstruction was performed using the state-of-the-art delay-and-sum image
 255 reconstruction with optimized receive f-number, correction of refraction at the soft tissue-bone
 256 interface and sample-specific wavespeed. A signal processing approach similar to the one adopted
 257 by [7] for in vivo imaging of the cortex of young adults were employed.

258 It is found that as Ct.Por increases, speckle intensity inside the bone cortex increases whereas
 259 the intensity of the signal from the endosteal interface decreases (Figure 8 and Figure 9). We found

260 a reduction of approximately 18 dB in endosteal visibility metric (C_{EI}) from the denser bones to the
 261 most degraded microstructures. Interestingly, the presence of large pores (quantified by Lg.Po.Dm
 262 and Dm.DC-9) and the width of the distribution of pore size (Dm.IDRng) had a strong effect on
 263 image contrast (see Table 2). For similar porosities, a microstructure with larger "large pores" will
 264 be associated to lower visibility of the endosteal interface (Figure 10). This means that the sole
 265 augmentation of cortical porosity is not enough to explain the contrast deterioration (see figure 11
 for illustration). Overall, the endosteal interface was visible ($C_{EI} > 0$ dB) for microstructures with

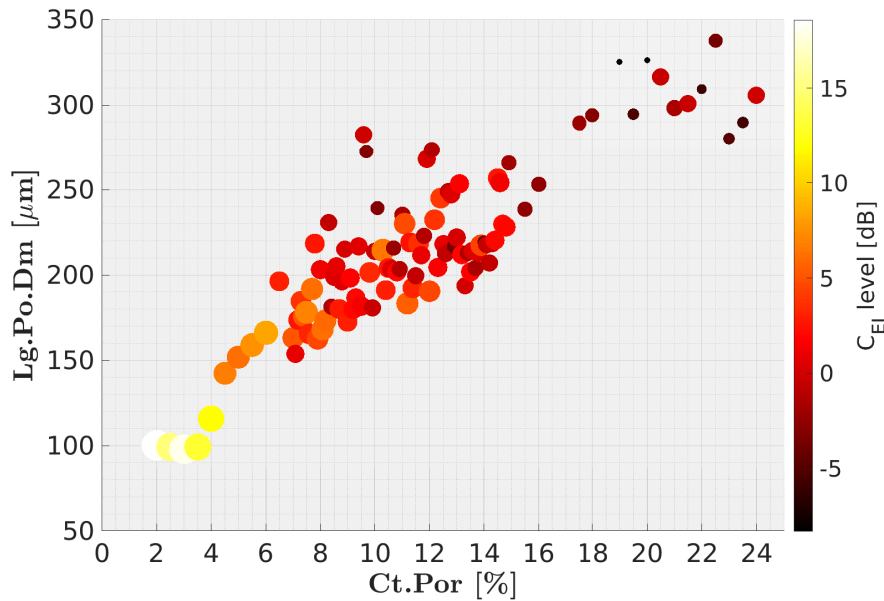


Figure 11: Scatter plot of endosteal interface contrast (C_{EI}) as a function of cortical porosity (Ct.Por) and diameter of large pore (Lg.Po.Dm). Size and color of each circle are proportional to the value of C_{EI}

266 moderate porosity (Ct.Por $\sim < 10\%$), small "large pore" size (Lg.Po.Dm $< 200 \mu\text{m}$), and weak pore
 267 size dispersion (Dm.IDRng $< 100 \mu\text{m}$). Endosteal interface was not visible ($C_{EI} < 0$ dB) for big
 268 "large pore" size (Lg.Po.Dm $> 250 \mu\text{m}$), high cortical porosity (Ct.Por $> 15\%$) and wide pore
 269 size dispersion (Dm.IDRng $> 170 \mu\text{m}$). These threshold values of the microstructure parameters
 270 are specific to our study as they are tied to the chosen central ultrasound frequency (2.5 MHz)
 271 used in vivo and cortical thickness (2.7 mm). For higher frequencies, ultrasound waves would
 272 experience stronger scattering by pores and higher attenuation resulting in lower threshold Ct.Por
 273 and Lg.Po.Dm values for a visible endosteum at the same depth.
 274

275 4.2. Possible physical origins of contrast loss

276 The failure to observe the endosteal interface for degraded microstructures may be explained
277 by several factors. The amplitude of the waves reflected at the endosteal interface decreases with
278 increasing porosity because the effective acoustic impedance mismatch between bone and marrow
279 is reduced. This can be quantified from the theoretical reflection coefficient (calculated for the
280 acoustic power) which drops by 25% (corresponding to -1.2 dB in an image, see Appendix D)
281 in the porosity range investigated. Therefore, the variations in the reflection coefficient cannot
282 explain the 8 dB decrease in the intensity of the endosteal interface (Figure 8). Another factor is
283 the attenuation that varies from about 20 dB/cm to 60 dB/cm in the investigated porosity range
284 (see Appendix E). This corresponds to a decrease in the amplitude of backscattered echoes of
285 about 20 dB if a round trip distance through the thickness of the cortex is considered. This value
286 is larger than the observed 8 dB reduction of the amplitude at the endosteal interface. Because
287 the proposed contrast metrics are calculated in the 0.8 mm-high regions of interest depicted in
288 Figure 6, it is likely that our approach cannot accurately track further decrease in the amplitude
289 of the specular reflection at the endosteal interface as the porosity increases. Indeed, because half
290 the region of interest of the endosteal interface encompasses cortical bone, the amplitude at the
291 endosteal interface shown in Figure 8 contains both specular reflection at the endosteal interface
292 and diffuse scattering by the pores near the endosteal interface. The main reason for the loss of
293 endosteal contrast could be the increase in the scattering strength from the inner microstructure
294 of the cortex as porosity increases. For a porosity larger than 15 %, the amplitude of echo signals
295 generated by the inner microstructure overcomes the amplitude of echo signals reflected at the
296 endosteal interface. As a consequence, the endosteal interface is no longer visible. As shown in
297 Figure 8, the speckle amplitude inside the cortex increases by about 10 dB (excluding extreme
298 values) as the porosity increases. The product ka where k is the wavenumber at central frequency
299 and for a wave speed of 3200 m/s, and a is the radius of the pores in the range 25 to 300 μm ,
300 varies from 0.12 to 1.5. Based on simulations similar to those of this study (but with monodisperse
301 circular pores), Iori et al [36] found an increase of the backscatter intensity of about 5 dB as ka
302 increased from 0.1 to 1, for ka between 1 and 1.5 a small decrease of about 2 dB was observed.
303 This increase of pore backscatter intensity with ka supports the idea that the presence of large
304 pores is the main cause of the loss of contrast at the endosteal interface.

305 *4.3. Design of the numerical study: motivations and advantages*

306 Our aim was to quantitatively assess the relationships between the bone microstructure and
307 image contrast. This study was conducted with numerical simulation for several reasons. Firstly,
308 this allowed us to investigate a large range of realistic microstructure types. This would not be
309 possible in an in vivo study due to the limitations in X-ray imaging resolution in vivo, nor in an
310 ex vivo study for which the number of samples and the control of their variability is an issue. One
311 strength of the present study is to use high resolution images of human cortical bone obtained
312 with SR- μ CT, which reveal the realistic details of the microstructure of human cortical bone.
313 Second, simulations of the imaging process are free of electronic noise and other experimental
314 artifacts, resulting in a best-case imaging scenario. Finally, a plate-like cortical thickness with
315 parallel interfaces was designed as the simplest imaging configuration to isolate the effect of varying
316 microstructure from those of varying thickness and interface curvature or interface tilt. Interface
317 curvature and tilt can be accounted for with the refraction corrected image reconstruction algorithm
318 used here [7].

319 *4.4. Limitations of the study*

320 The original microstructure images obtained with SR- μ CT were relatively small (2.7×3.5 mm²).
321 Other high resolution imaging modalities could have been used to generate the model, such as
322 scanning acoustic microscopy [37]. The advantage of using SR- μ CT images was the high resolution
323 (voxel size of 6.5 μ m) and high contrast providing an accurate picture of the pores. Although the
324 vast majority of simulations of ultrasound propagation in cortical bone has been conducted in
325 2D configurations in the plane transverse to osteons [8, 26], the validity of this configuration has
326 not been investigated in detail. Haversian canals are not infinite cylinders as hypothesized here
327 but their average length is in the range of 2-4 mm [38]. Volkmann canals, which run nearly
328 perpendicular to Haversian canals, contribute to a part of the porosity and are not modeled in 2D
329 configurations. Another three-dimensional feature not considered here is the spatial resolution in
330 the elevation dimension of the probe which is finite and results in a summation of the backscattered
331 signals over the height of the elements of the probe array. In cortical bone, attenuation due to pore
332 scattering and absorption within the bone solid matrix both contribute to the total attenuation
333 coefficient. In these simulations, a frequency-independent absorption within the bone matrix is
334 modeled with an absorption coefficient of 19.0 dB/cm at 2.5 MHz following Yousefian et al. [18],
335 [25]. This value leads to a total attenuation slightly higher than the values reported by Grimal

336 et al [39] from ex-vivo measurements of attenuation in human cortical bone specimens. They
337 reported an attenuation of about 50 dB/cm at 4 MHz for specimens with a porosity around 10%
338 while in the present simulation study we found an attenuation of 40 dB/cm at 2.5 MHz for the
339 same porosity (see Appendix E). Some simulations were also conducted without absorption within
340 the bone matrix (results not shown) and the results were found to be similar. Accordingly, we
341 believe that the conclusions of this study are not sensitive to the choice of the absorption coefficient
342 in the matrix. Finally, the heterogeneity of the distribution pore sizes was not fully considered.
343 Specifically, a gradient of pore sizes through the cortex was only present in a few microstructure
344 images, and the roughness of the endosteal interface due to the presence of large pores across
345 the interface (trabecularization) [40] was not considered. The impact on image quality of this
346 heterogeneity should be investigated in a separate study.

347 *4.5. Conclusion and perspectives*

348 The simulation results presented in this article suggest that the cortical thickness of individuals
349 with low and moderate porosity can be successfully imaged at 2.5 MHz. This is in line with the
350 in vivo results of Renaud et al. [7] on two young subjects for which the endosteal interface could
351 be clearly identified at the radius and tibia. In contrast, our results suggest that imaging the
352 cortical bone of some elderly subjects or osteoporotic subjects with a degraded microstructure
353 (porosity larger than 10%, presence of large pores) [14] would be challenging. Specifically, we
354 have found that the presence of large pores is detrimental to image quality. Such large pores
355 are characteristic of degraded bone and were associated with weak femoral strength ex vivo [35]
356 and with fracture risk [41]. This may appear to be a major obstacle to bone imaging for some
357 individuals with a high risk of fracture. A central frequency of 2.5 MHz like in in vivo measurements
358 [7] is used. With a lower frequency, scattering and absorption may be reduced, however the
359 spatial resolution in the ultrasound image may be not sufficient to clearly distinguish the endosteal
360 interface from the periosteal and measure the cortical thickness. In this study we have used
361 an optimally-implemented delay-and-sum image reconstruction algorithm, and demonstrated the
362 limits of this approach. Advanced signal processing and image reconstruction could be considered
363 to overcome this limitation, including data adaptive beamforming, specular beamforming, inverse
364 problem and machine learning approaches [42, 43, 44, 45].

365 **Appendix A Estimating the bone matrix characteristics**

366 The material properties of the bone matrix tissue used for the numerical simulations of the
 367 propagation of elastic waves were derived from experimental data as described below.

Mass density. The bone matrix mass density (ρ^m) was deduced from measurements of the ap-
 parent mass density (ρ) and cortical porosity (Ct.Por) of 55 cortical bone specimens from elderly
 donors [33] (the microstructures used in the present study came from the same samples). A linear
 regression between ρ and Ct.Por is determined:

$$\rho = \rho^m - 13.1 \times \text{Ct.Por}$$

368 where ρ^m is the intercept for a null porosity. The correlation between ρ and Ct.Por was strong:
 369 $\text{Adj-R}^2 = 84.5 \%$, $p = 2.43 \cdot 10^{-23}$, $\text{RMSE} = 22.1 \text{ kg.m}^{-3}$. Finally, a value of 1996 kg.m^{-3} was found
 370 for ρ^m . Figure A.12 shows the values of ρ as a function of cortical porosity along with the linear
 fit.

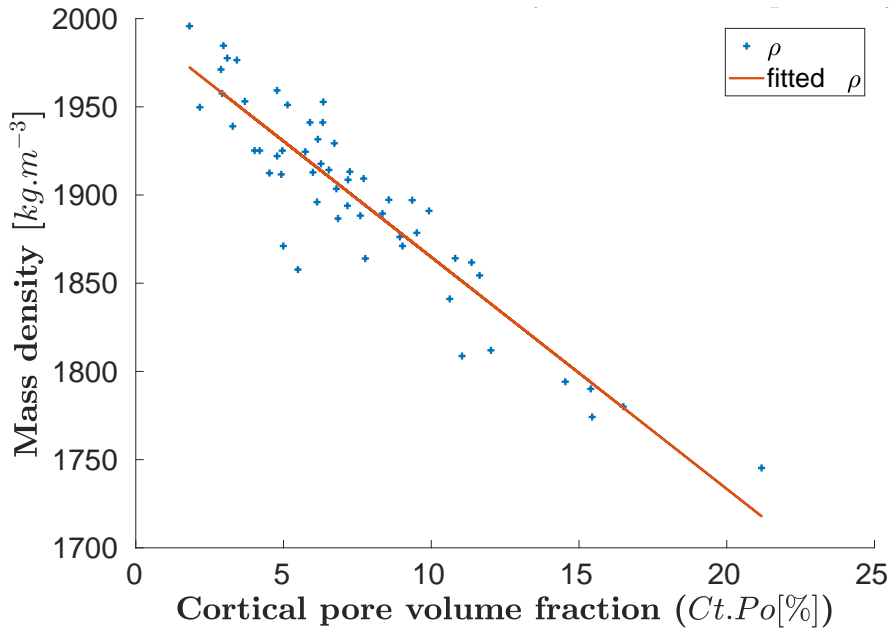


Figure A.12: Cortical bone apparent mass density (ρ) of the 55 human bone specimens of this study obtained by [33]. A regression linear model is fitted (red line).

371

Shear and compressional wave-speeds. Longitudinal and shear wave speeds in the bone matrix are deduced from ρ^m and experimental values of the matrix elastic coefficients C_{ij}^m (using Voigt notation, with $i, j = 1, 2, 3$) provided by Cai et al.[33] for the same bone specimens. For this study,

V_1^m and V_{12}^m were used, they are respectively the velocities of longitudinal and compressional waves propagating in bone matrix in the plane perpendicular to the bone axis and with in-plane particle motion. They are determined using:

$$V_1^m = \sqrt{\frac{C_{11}^m}{\rho^m}}, \quad \text{and} \quad V_{12}^m = \sqrt{\frac{C_{66}^m}{\rho^m}}.$$

372 Cai et al. [33] reported $C_{11}^m = 24.5$ GPa and $C_{66}^m = 5.4$ GPa, from which values of 3496 m.s^{-1} and
 373 1645 m.s^{-1} were deduced for V_1^m and V_{12}^m respectively.

374 Appendix B Experimental ultrasonic velocity estimation for different cortical porosi- 375 ties

376 Cai et al [20] measured the stiffness tensor (C_{ij}), apparent mass density (ρ), and vascular
 377 porosity of cortical bone specimens from elderly donors. The compressional wave-speed for each
 378 specimen was calculated as $\sqrt{\frac{C_{11}}{\rho}}$, where C_{11} is the specimen-specific elastic coefficient correspond-
 379 ing to longitudinal deformation in the plane of isotropy. The obtained values of wave-speed in
 380 direction 1 (any direction normal to the symmetry axis of the microstructure) as a function of the
 381 intra-cortical porosity are shown in Figure 7 in blue diamonds. The red circles in Figure 7 represent
 382 the values of wave-speed estimated from this study using the method described in section 2.4 and
 the configuration of Figure B.13.

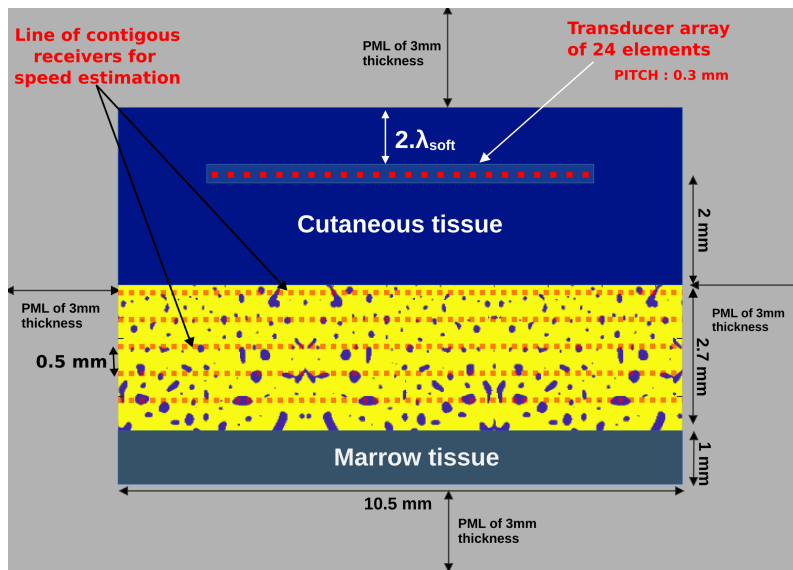


Figure B.13: Configuration model used for estimation of wave-speed in cortical bone. Virtual receivers are placed inside bone along 5 equally spaced (spacing=0.5 mm) lines (red dotted line inside cortical bone layer).

384 **Appendix C Determination of the optimal receive f-number for endosteal detection**

385 In order to use the DAS algorithm optimally, the receive f-number was optimized as explained
 386 by Perrot et al. [32]. The interface visibility is evaluated for 25 different f-number values ranging
 387 from 0.2 to 2.6. The f-number was constant throughout the image, resulting in a different number
 388 of elements used for each point of the image. For a f-number greater than 2.6, less than 3 elements
 389 are used for the reconstruction of the endosteal interface, therefore the f-number was studied for
 390 values lower than 2.6. For a configuration without cortical pores (Ct.Por=0%), C_{EP} (defined in
 391 section 2.6) increases with f-number and reaches its maximum for a f-number close to 1.9 (increase
 392 of 8 dB). This is illustrated in Figure C.14.

Globally, the f-number that maximizes C_{EP} is close to 1.9. This value of f-number corresponds

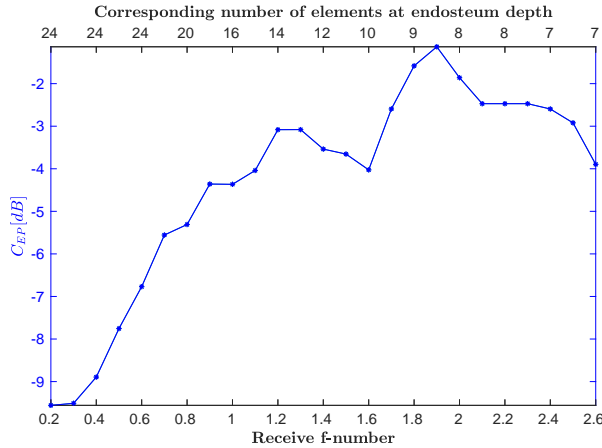


Figure C.14: Endosteum-Periosteum contrast for different values of f-number for a configuration without microstructure (i.e. porosity= 0%). The number of active elements is also given.

393 to a receive aperture of 2.35 mm equivalent to 9 active elements for a focusing depth of 4.7 mm
 394 (i.e at the endosteal interface). For C_{EI} , the increase of contrast is smaller (increase of 3 dB), but
 395 the tendency is the same as for C_{EP} for almost all configurations. The f-number that maximizes
 396 C_{EI} is also close to 1.9. The metrics decrease for large f-number values.

398 Figure C.15 is an example plot of endosteal interface visibility against f-number for a configuration
 399 with a cortical porosity of 5.5%.

400

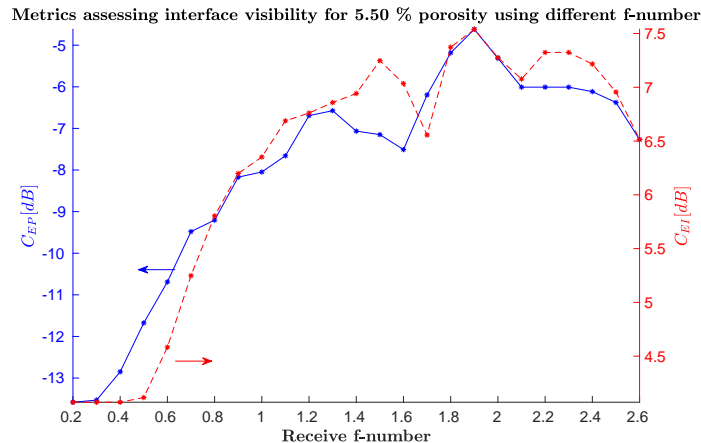


Figure C.15: Quantitative assessment of endosteal interface visibility as a function of the f-number, for a microstructure with a porosity of 5.5% porosity. The blue solid curve is relative interface contrast (C_{EP}) and the red dashed curve is endosteal interface contrast (C_{EI}).

401 Appendix D Power reflection coefficient at the endosteal surface.

The amplitude of the specular reflection is important to interpret the appearance of the interfaces in the images of this study. Therefore the power reflection coefficient at the endosteal surface were calculated for different microstructure. As porosity increases, the speed of sound in cortical bone decreases leading to a drop of the power reflection coefficient at endosteal interface (R_{end}). The theoretical power reflection coefficient of plane waves is:

$$R_{end} = \left(\frac{Z_{marrow} - Z_{bone}}{Z_{marrow} + Z_{bone}} \right)^2,$$

402 where Z_{marrow} and Z_{bone} are the impedances of marrow and bone. In Figure D.16, reports R_{end} as
 403 a function of cortical porosity. In the porosity range 2-24 %, R_{end} decreases by 25 % of its value
 404 at 2 % porosity.

405 Appendix E Attenuation coefficient

Estimation of the ultrasonic attenuation coefficient with numerical simulations. The attenuation value is important to interpret the ultrasound images of cortical bone obtained in this study. Therefore an analysis were conducted to document the variation of attenuation for our samples. Beside absorption inside the bone matrix, scattering due to pores contributes to the total amount of attenuation. To estimate the total attenuation coefficient in cortical bone additional simulation mimicking the substitution method commonly used for the experimental characterization of attenuation [46] were performed. For each model (i.e. each microstructure, see Figure 3), a plane wave

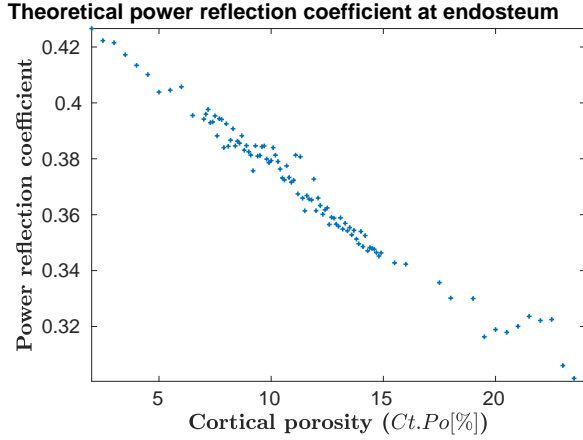


Figure D.16: Plane wave power reflection coefficient at the endosteal interface for each cortical microstructure.

at normal incidence is emitted by the transducer array and recorded after propagation through the layer of cortical bone by a line of virtual receivers positioned slightly below and parallel to the endosteal interface. To obtain a reference signal, the bone tissue is replaced with soft tissue. The attenuation coefficient in cortical bone was derived from the ratio of the magnitude spectrum of the signal received after propagation through bone ($|S(f)|$) to the magnitude spectrum of the reference signal ($|S_0(f)|$). Losses due to transmission through the two interfaces of the cortical bone layer were taken into account using the values of the plane wave transmission coefficients T_p (through the periosteal interface) and T_e (through the endosteal interface) calculated from the estimated compressional wave-speed (V_1) and apparent mass density (ρ). The attenuation coefficient α_{dB} in cortical bone expressed in dB/cm is obtained from:

$$\alpha_{dB}(f) = \frac{20}{\ln(10)} \frac{1}{Ct.Th} \ln\left(\frac{|S_0(f)|T_pT_e}{|S(f)|}\right)$$

406 , where Ct.Th is the thickness of the cortical bone layer in cm (0.27 cm).

407 Two sets of simulation were performed: with and without absorption in the bone matrix.
 408 Absorption in the bone matrix was set to 19.05 dB/cm as explained in Materials and Methods.
 409 Figure E.17 shows the obtained attenuation coefficient values as a function of porosity.

410

411

412 *Relationship with microstructure.* The difference between attenuation coefficients for simulations
 413 with and without bone matrix absorption is close to 19 dB/cm as expected. In fact, in this
 414 study, the maximum normalized frequency calculated as the product of sample wavenumber(k) and

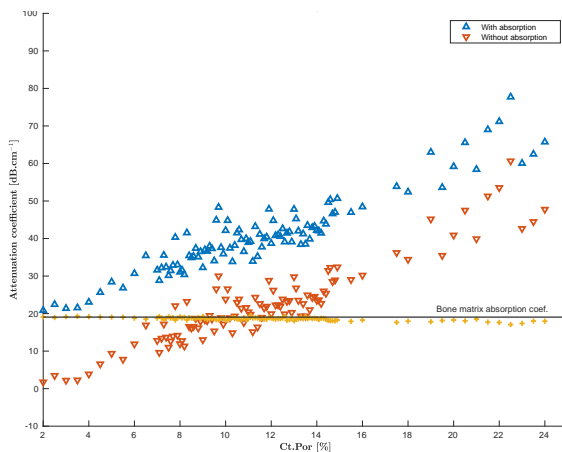


Figure E.17: Ultrasonic attenuation coefficient at 2.5 MHz in cortical bone as a function of porosity for simulations with absorption in bone matrix (blue upward pointing triangles) and simulations without absorption (red downward pointing triangles). The difference between these two data sets is also shown as yellow crosses.

415 sample median pore diameter (Ct.Po.Dm) is 0.66 (moderate scattering regime), therefore, total
 416 attenuation is expected to be a linear summation of the bone matrix absorption and attenuation
 417 due to scattering [25].

418 Scattering attenuation coefficient is highly influenced by cortical microstructure. In the porosity
 range (2-24 %), attenuation coefficient increased by 40 dB/cm (Figure E.17). Spearman rank

	Lg.Po.Dm	Ct.Por	Dm.DC-9	Dm.IDRng	Ct.Po.Dm	Dm.Rng	Dm.DC-1	Sm.Po.Dm	Ct.Po.Dn
Attenuation coefficient	0.92 ²	0.89 ²	0.83 ²	0.82 ²	0.70 ²	0.67 ¹	0.54 ²	0.46 ²	-0.21 ^{n.s}

Table E.3: Spearman correlation coefficient r_s between attenuation coefficient and microstructure properties (see 2.2 for the definition of variables). ^{n.s}: not significant $p > 0.05$, ¹: $0.001 < p < 0.05$, ²: $p < 0.001$

419 correlation coefficient between attenuation and microstructure variables were evaluated. There
 420 was strong positive correlation coefficient (r_s) for large pore size ($r_s = 0.92$), porosity ($r_s = 0.89$
 421) and 9th decile of diameters ($r_s = 0.83$) (see Table E.3). These statistics suggest that scattering
 422 magnitude increases with pore size and is dominated by scattering caused by large pores.
 423

424 Appendix F Large pore influence on the visibility of the endosteal interface

425 Figure F.18 illustrates pore size effect on the visibility of the endosteal interface. The SR- μ CT
 426 images of microstructures correspond to the reconstructed images of Figure 10. In the leftmost im-
 427 age, the microstructure does not contain pores with large diameter (Lg.Po.Dm=183.3 μ m) and the

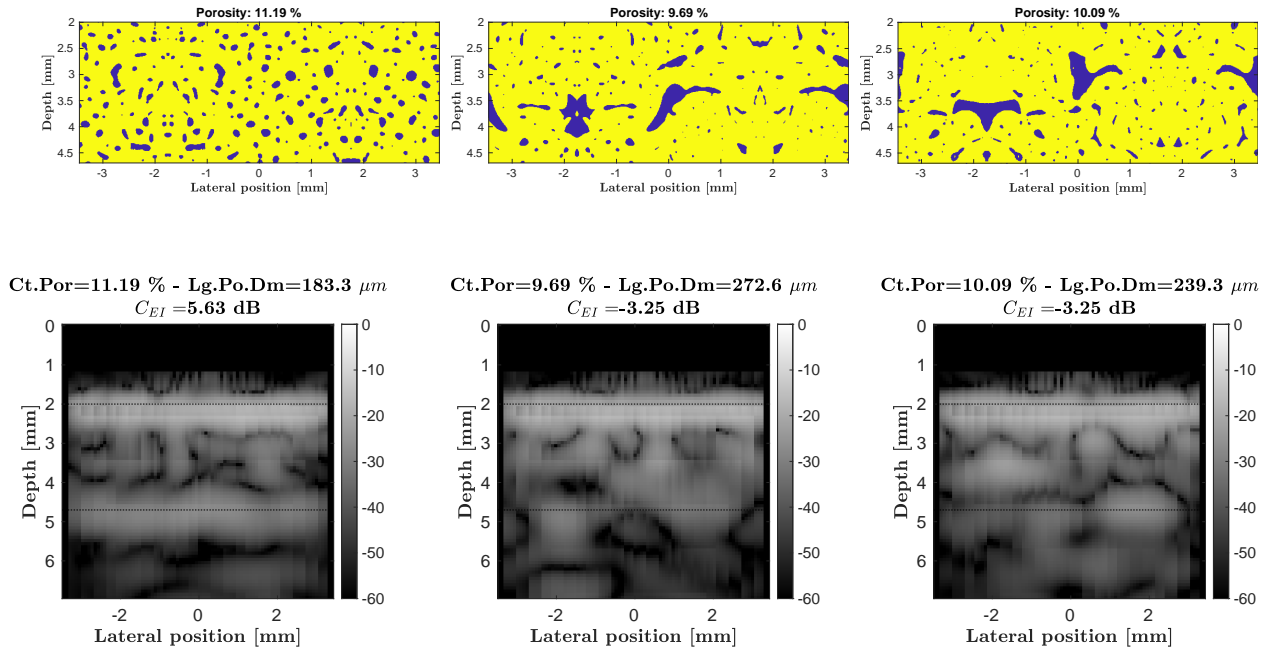


Figure F.18: Binarized SR- μ CT image of microstructure with similar porosities (top) but increasing large pore size and their corresponding reconstructed ultrasound images (down).

428 endosteal interface is clearly visible ($C_{EI} = 5.63$ dB) while in the two following images some large
 429 pores (Lg.Po.Dm=272.6 μ m and Lg.Po.Dm=239.3 μ m) are observed and the endosteal interface is
 430 not visible ($C_{EI} = -3.25$ dB for both).

431 References

- 432 [1] C. Cooper, S. L. Ferrari, IOF Compendium of Osteoporosis Publisher: International Osteo-
 433 porosis Foundation (IOF) (2017).
 434 URL <https://archive-ouverte.unige.ch/unige:125569>
- 435 [2] E. S. Siris, Y.-T. Chen, T. A. Abbott, E. Barrett-Connor, P. D. Miller, L. E. Wehren, M. L.
 436 Berger, Bone Mineral Density Thresholds for Pharmacological Intervention to Prevent Frac-
 437 tures, Archives of Internal Medicine 164 (10) (2004) 1108–1112. doi:10.1001/archinte.
 438 164.10.1108.
 439 URL <https://doi.org/10.1001/archinte.164.10.1108>
- 440 [3] K. Briot, S. Paternotte, S. Kolta, R. Eastell, D. Felsenberg, D. M. Reid, C.-C. Glüer,
 441 C. Roux, FRAX[®]: Prediction of Major Osteoporotic Fractures in Women from the General

- 442 Population: The OPUS Study, PLOS ONE 8 (12) (2013) e83436, publisher: Public Library
443 of Science. doi:10.1371/journal.pone.0083436.
444 URL [https://journals.plos.org/plosone/article?id=10.1371/journal.pone.](https://journals.plos.org/plosone/article?id=10.1371/journal.pone.0083436)
445 0083436
- 446 [4] P. Laugier, Q. Grimal, Bone Quantitative Ultrasound: New Horizons, 1st Edition, no. 1364
447 in Advances in Experimental Medicine and Biology, Springer International Publishing, 2022.
- 448 [5] Q. Grimal, P. Laugier, Quantitative Ultrasound Assessment of Cortical Bone Properties Be-
449 yond Bone Mineral Density, IRBM 40 (1) (2019) 16–24. doi:10.1016/j.irbm.2018.10.006.
450 URL <https://www.sciencedirect.com/science/article/pii/S1959031818301982>
- 451 [6] V. Beltrame, R. Stramare, N. Rebellato, F. Angelini, A. C. Frigo, L. Rubaltelli, Sonographic
452 evaluation of bone fractures: a reliable alternative in clinical practice?, Clinical Imaging 36 (3)
453 (2012) 203–208. doi:10.1016/j.clinimag.2011.08.013.
454 URL <https://www.sciencedirect.com/science/article/pii/S0899707111001732>
- 455 [7] G. Renaud, P. Kruizinga, D. Cassereau, P. Laugier, In vivo ultrasound imaging of the bone
456 cortex, Physics in Medicine & Biology 63 (12) (2018) 125010, publisher: IOP Publishing.
457 doi:10.1088/1361-6560/aac784.
458 URL <https://doi.org/10.1088%2F1361-6560%2Faac784>
- 459 [8] H. Nguyen Minh, J. Du, K. Raum, Estimation of Thickness and Speed of Sound in Corti-
460 cal Bone Using Multifocus Pulse-Echo Ultrasound, IEEE transactions on ultrasonics, ferro-
461 electrics, and frequency control 67 (3) (2020) 568–579. doi:10.1109/TUFFC.2019.2948896.
- 462 [9] P. Augat, S. Schorlemmer, The role of cortical bone and its microstructure in bone strength,
463 Age and Ageing 35 (suppl_2) (2006) ii27–ii31. doi:10.1093/ageing/af1081.
464 URL <https://doi.org/10.1093/ageing/af1081>
- 465 [10] Y. Bala, R. Zebaze, E. Seeman, Role of cortical bone in bone fragility, Current Opinion in
466 Rheumatology 27 (4) (2015) 406–413. doi:10.1097/BOR.000000000000183.
467 URL [https://journals.lww.com/co-rheumatology/Abstract/2015/07000/Role_of_](https://journals.lww.com/co-rheumatology/Abstract/2015/07000/Role_of_cortical_bone_in_bone_fragility.13.aspx)
468 [cortical_bone_in_bone_fragility.13.aspx](https://journals.lww.com/co-rheumatology/Abstract/2015/07000/Role_of_cortical_bone_in_bone_fragility.13.aspx)

- 469 [11] K. L. Bell, N. Loveridge, J. Power, N. Garrahan, B. F. Meggitt, J. Reeve, Regional differences
470 in cortical porosity in the fractured femoral neck, *Bone* 24 (1) (1999) 57–64. doi:10.1016/
471 S8756-3282(98)00143-4.
472 URL <https://www.sciencedirect.com/science/article/pii/S8756328298001434>
- 473 [12] C. M. Andreasen, J.-M. Delaisse, B. C. van der Eerden, J. P. van Leeuwen, M. Ding,
474 T. L. Andersen, Understanding Age-Induced Cortical Porosity in Women: The Accu-
475 mulation and Coalescence of Eroded Cavities Upon Existing Intracortical Canals Is the
476 Main Contributor, *Journal of Bone and Mineral Research* 33 (4) (2018) 606–620, _eprint:
477 <https://onlinelibrary.wiley.com/doi/pdf/10.1002/jbmr.3354>. doi:10.1002/jbmr.3354.
478 URL <https://onlinelibrary.wiley.com/doi/abs/10.1002/jbmr.3354>
- 479 [13] V. Bousson, A. Meunier, C. Bergot, E. Vicaut, M. A. Rocha, M. H. Morais, A.-M. Laval-
480 Jeantet, J.-D. Laredo, Distribution of Intracortical Porosity in Human Midfemoral Cortex
481 by Age and Gender, *Journal of Bone and Mineral Research* 16 (7) (2001) 1308–1317. doi:
482 10.1359/jbmr.2001.16.7.1308.
483 URL <https://onlinelibrary.wiley.com/doi/abs/10.1359/jbmr.2001.16.7.1308>
- 484 [14] D. M. L. Cooper, C. D. L. Thomas, J. G. Clement, A. L. Turinsky, C. W. Sensen, B. Hall-
485 grímsson, Age-dependent change in the 3D structure of cortical porosity at the human femoral
486 midshaft, *Bone* 40 (4) (2007) 957–965. doi:10.1016/j.bone.2006.11.011.
487 URL <https://www.sciencedirect.com/science/article/pii/S8756328206008465>
- 488 [15] C. Chappard, S. Bensalah, C. Olivier, P. J. Gouttenoire, A. Marchadier, C. Benhamou,
489 F. Peyrin, 3D characterization of pores in the cortical bone of human femur in the elderly
490 at different locations as determined by synchrotron micro-computed tomography images, *Osteoporosis international: a journal established as result of cooperation between the European*
491 *Foundation for Osteoporosis and the National Osteoporosis Foundation of the USA* 24 (3)
492 (2013) 1023–1033. doi:10.1007/s00198-012-2044-4.
493
- 494 [16] K. Raum, I. Leguerney, F. Chandelier, M. Talmant, A. Saïed, F. Peyrin, P. Laugier, Site-
495 matched assessment of structural and tissue properties of cortical bone using scanning acoustic
496 microscopy and synchrotron radiation μ CT, *Physics in Medicine and Biology* 51 (3)

- 497 (2006) 733–746, publisher: IOP Publishing. doi:10.1088/0031-9155/51/3/017.
498 URL <https://doi.org/10.1088/0031-9155/51/3/017>
- 499 [17] M. S. Stein, S. A. Feik, C. D. L. Thomas, J. G. Clement, J. D. Wark,
500 An Automated Analysis of Intracortical Porosity in Human Femoral Bone Across
501 Age, *Journal of Bone and Mineral Research* 14 (4) (1999) 624–632, _eprint:
502 <https://onlinelibrary.wiley.com/doi/pdf/10.1359/jbmr.1999.14.4.624>. doi:10.1359/jbmr.
503 1999.14.4.624.
504 URL <https://onlinelibrary.wiley.com/doi/abs/10.1359/jbmr.1999.14.4.624>
- 505 [18] O. Yousefian, R. D. White, Y. Karbalaeeisadegh, H. T. Banks, M. Muller, The effect of pore
506 size and density on ultrasonic attenuation in porous structures with mono-disperse random
507 pore distribution: A two-dimensional in-silico study, *The Journal of the Acoustical Society of*
508 *America* 144 (2) (2018) 709. doi:10.1121/1.5049782.
- 509 [19] M. P. Zamorani, M. Valle, Bone and Joint, in: S. Bianchi, C. Martinoli (Eds.), *Ultrasound*
510 *of the Musculoskeletal System*, Medical Radiology, Springer, Berlin, Heidelberg, 2007, pp.
511 137–185. doi:10.1007/978-3-540-28163-4_5.
512 URL https://doi.org/10.1007/978-3-540-28163-4_5
- 513 [20] X. Cai, H. Follet, L. Peralta, M. Gardegaront, D. Farlay, R. Gauthier, B. Yu, E. Gineyts,
514 C. Olivier, M. Langer, A. Gourrier, D. Mitton, F. Peyrin, Q. Grimal, P. Laugier, Anisotropic
515 elastic properties of human femoral cortical bone and relationships with composition and
516 microstructure in elderly, *Acta Biomaterialia* 90 (2019) 254–266. doi:10.1016/j.actbio.
517 2019.03.043.
518 URL <https://www.sciencedirect.com/science/article/pii/S1742706119302181>
- 519 [21] X. Cai, R. Brenner, L. Peralta, C. Olivier, P.-J. Gouttenoire, C. Chappard, F. Peyrin,
520 D. Cassereau, P. Laugier, Q. Grimal, Homogenization of cortical bone reveals that the organi-
521 zation and shape of pores marginally affect elasticity, *Journal of The Royal Society Interface*
522 16 (151) (2019) 20180911, publisher: Royal Society. doi:10.1098/rsif.2018.0911.
523 URL <https://royalsocietypublishing.org/doi/10.1098/rsif.2018.0911>
- 524 [22] C. M. Moran, N. L. Bush, J. C. Bamber, Ultrasonic propagation properties of excised
525 human skin, *Ultrasound in Medicine & Biology* 21 (9) (1995) 1177–1190. doi:10.1016/

- 526 0301-5629(95)00049-6.
527 URL <https://www.sciencedirect.com/science/article/pii/0301562995000496>
- 528 [23] S. Kawasaki, R. Ueda, A. Hasegawa, A. Fujita, T. Mihata, M. Matsukawa, M. Neo, Ultrasonic
529 wave properties of human bone marrow in the femur and tibia, *The Journal of the Acoustical*
530 *Society of America* 138 (1) (2015) EL83–EL87. doi:10.1121/1.4922764.
531 URL <https://asa.scitation.org/doi/10.1121/1.4922764>
- 532 [24] R. Lakes, H. S. Yoon, J. Lawrence Katz, Ultrasonic wave propagation and attenuation in wet
533 bone, *Journal of Biomedical Engineering* 8 (2) (1986) 143–148. doi:10.1016/0141-5425(86)
534 90049-X.
535 URL <https://www.sciencedirect.com/science/article/pii/014154258690049X>
- 536 [25] O. Yousefian, Y. Karbalaieisadegh, M. Muller, Frequency-dependent analysis of ultrasound
537 apparent absorption coefficient in multiple scattering porous media: application to cortical
538 bone, *Physics in Medicine & Biology* 66 (3) (2021) 035026. doi:10.1088/1361-6560/abb934.
539 URL <https://doi.org/10.1088/1361-6560/abb934>
- 540 [26] K. Mohanty, O. Yousefian, Y. Karbalaieisadegh, M. Ulrich, Q. Grimal, M. Muller, Artificial
541 neural network to estimate micro-architectural properties of cortical bone using ultrasonic
542 attenuation: A 2-D numerical study, *Computers in Biology and Medicine* 114 (2019) 103457.
543 doi:10.1016/j.combiomed.2019.103457.
544 URL <http://www.sciencedirect.com/science/article/pii/S0010482519303312>
- 545 [27] Y. Karbalaieisadegh, O. Yousefian, G. Iori, K. Raum, M. Muller, Acoustic diffusion constant
546 of cortical bone: Numerical simulation study of the effect of pore size and pore density on
547 multiple scattering, *The Journal of the Acoustical Society of America* 146 (2) (2019) 1015–
548 1023, publisher: Acoustical Society of America. doi:10.1121/1.5121010.
549 URL <https://asa.scitation.org/doi/10.1121/1.5121010>
- 550 [28] E. Bossy, SimSonic: free ftd software for the simulation of ultrasonic waves propagation.
551 URL <http://www.simsonic.fr/>
- 552 [29] E. Bossy, F. Padilla, F. Peyrin, P. Laugier, Three-dimensional simulation of ultrasound
553 propagation through trabecular bone structures measured by synchrotron microtomogra-
554 phy, *Physics in Medicine and Biology* 50 (23) (2005) 5545–5556, publisher: IOP Publishing.

555 doi:10.1088/0031-9155/50/23/009.

556 URL <https://doi.org/10.1088/0031-9155/50/23/009>

557 [30] E. Bossy, Q. Grimal, Numerical Methods for Ultrasonic Bone Characterization, in: P. Laugier,
558 G. Haiat (Eds.), Bone Quantitative Ultrasound, Springer Netherlands, Dordrecht, 2011, pp.
559 181–228. doi:10.1007/978-94-007-0017-8_8.

560 URL https://doi.org/10.1007/978-94-007-0017-8_8

561 [31] Q. Grimal, K. Raum, A. Gerisch, P. Laugier, A determination of the minimum sizes of repre-
562 sentative volume elements for the prediction of cortical bone elastic properties, Biomechanics
563 and Modeling in Mechanobiology 10 (6) (2011) 925–937. doi:10.1007/s10237-010-0284-9.

564 URL <https://doi.org/10.1007/s10237-010-0284-9>

565 [32] V. Perrot, M. Polichetti, F. Varray, D. Garcia, So you think you can DAS? A viewpoint on
566 delay-and-sum beamforming, Ultrasonics 111 (2021) 106309. doi:10.1016/j.ultras.2020.
567 106309.

568 URL <https://www.sciencedirect.com/science/article/pii/S0041624X20302444>

569 [33] X. Cai, L. Peralta, R. Brenner, G. Iori, D. Cassereau, K. Raum, P. Laugier, Q. Gri-
570 mal, Anisotropic elastic properties of human cortical bone tissue inferred from inverse ho-
571 mogenization and resonant ultrasound spectroscopy, Materialia 11 (2020) 100730. doi:
572 10.1016/j.mtla.2020.100730.

573 URL <https://www.sciencedirect.com/science/article/pii/S2589152920301472>

574 [34] L. Peralta, J. D. Maeztu Redin, F. Fan, X. Cai, P. Laugier, J. Schneider, K. Raum, Q. Gri-
575 mal, Bulk wave velocities in cortical bone reflect porosity and compression strength, Ultra-
576 sound in Medicine & Biology 47 (3) (2021) 799–808. doi:[https://doi.org/10.1016/j.](https://doi.org/10.1016/j.ultrasmedbio.2020.11.012)
577 [ultrasmedbio.2020.11.012](https://doi.org/10.1016/j.ultrasmedbio.2020.11.012).

578 URL <https://www.sciencedirect.com/science/article/pii/S0301562920305202>

579 [35] G. Iori, J. Schneider, A. Reisinger, F. Heyer, L. Peralta, C. Wyers, M. Gräsel, R. Barkmann,
580 C. C. Glüer, J. P. v. d. Bergh, D. Pahr, K. Raum, Large cortical bone pores in the tibia
581 are associated with proximal femur strength, PLOS ONE 14 (4) (2019) e0215405, publisher:
582 Public Library of Science. doi:10.1371/journal.pone.0215405.

- 583 URL [https://journals.plos.org/plosone/article?id=10.1371/journal.pone.](https://journals.plos.org/plosone/article?id=10.1371/journal.pone.0215405)
584 0215405
- 585 [36] G. Iori, J. Du, J. Hackenbeck, V. Kilappa, K. Raum, Estimation of Cortical Bone Microstruc-
586 ture from Ultrasound Backscatter, *IEEE Transactions on Ultrasonics, Ferroelectrics, and*
587 *Frequency Control* (2020) 1–1Conference Name: *IEEE Transactions on Ultrasonics, Ferro-*
588 *electrics, and Frequency Control.* doi:10.1109/TUFFC.2020.3033050.
- 589 [37] Q. Grimal, D. Rohrbach, J. Grondin, R. Barkmann, C.-C. Glüer, K. Raum, P. Laugier, Mod-
590 eling of Femoral Neck Cortical Bone for the Numerical Simulation of Ultrasound Propagation,
591 *Ultrasound in Medicine & Biology* 40 (5) (2014) 1015–1026. doi:10.1016/j.ultrasmedbio.
592 2013.11.010.
593 URL <https://linkinghub.elsevier.com/retrieve/pii/S0301562913011538>
- 594 [38] D. M. L. Cooper, C. E. Kawalilak, K. Harrison, B. D. Johnston, J. D. Johnston, Cortical Bone
595 Porosity: What Is It, Why Is It Important, and How Can We Detect It?, *Current Osteoporosis*
596 *Reports* 14 (5) (2016) 187–198. doi:10.1007/s11914-016-0319-y.
597 URL <https://doi.org/10.1007/s11914-016-0319-y>
- 598 [39] Q. Grimal, M. Talmant, G. Renaud, Measurement of ultrasonic anisotropic attenuation of
599 P-wave in millimetric-sized human cortical bone samples [abstract], *International Symposium*
600 *on Ultrasonic Characterisation of Bone* (2019, Villa-Clythia, Fréjus, France) 1.
- 601 [40] R. M. Zebaze, A. Ghasem-Zadeh, A. Bohte, S. Iuliano-Burns, M. Mirams, R. I. Price, E. J.
602 Mackie, E. Seeman, Intracortical remodelling and porosity in the distal radius and post-
603 mortem femurs of women: a cross-sectional study, *The Lancet* 375 (9727) (2010) 1729–1736.
604 doi:10.1016/S0140-6736(10)60320-0.
605 URL <https://www.sciencedirect.com/science/article/pii/S0140673610603200>
- 606 [41] G. Armbrecht, H. Nguyen Minh, J. Massmann, K. Raum, Pore-Size Distribution and
607 Frequency-Dependent Attenuation in Human Cortical Tibia Bone Discriminate Fragility Frac-
608 tures in Postmenopausal Women With Low Bone Mineral Density, *JBMR Plus* 5 (11) (2021)
609 e10536. doi:10.1002/jbm4.10536.
610 URL <https://onlinelibrary.wiley.com/doi/abs/10.1002/jbm4.10536>

- 611 [42] H. Hasegawa, Recent Developments in Adaptive Beamforming, in: 2019 IEEE International
612 Ultrasonics Symposium (IUS), 2019, pp. 1063–1066, iSSN: 1948-5727. doi:10.1109/ULTSYM.
613 2019.8925830.
- 614 [43] A. Rodriguez-Molares, A. Fatemi, L. Løvstakken, H. Torp, Specular Beamforming, IEEE
615 Transactions on Ultrasonics, Ferroelectrics, and Frequency Control 64 (9) (2017) 1285–1297,
616 conference Name: IEEE Transactions on Ultrasonics, Ferroelectrics, and Frequency Control.
617 doi:10.1109/TUFFC.2017.2709038.
- 618 [44] R. Lavarello, F. Kamalabadi, W. O’Brien, A regularized inverse approach to ultrasonic pulse-
619 echo imaging, IEEE Transactions on Medical Imaging 25 (6) (2006) 712–722, conference Name:
620 IEEE Transactions on Medical Imaging. doi:10.1109/TMI.2006.873297.
- 621 [45] S. Liu, Y. Wang, X. Yang, B. Lei, L. Liu, S. X. Li, D. Ni, T. Wang, Deep Learning in Medical
622 Ultrasound Analysis: A Review, Engineering 5 (2) (2019) 261–275. doi:10.1016/j.eng.
623 2018.11.020.
624 URL <https://www.sciencedirect.com/science/article/pii/S2095809918301887>
- 625 [46] M. Sasso, G. Haïat, Y. Yamato, S. Naili, M. Matsukawa, Frequency Dependence of Ultrasonic
626 Attenuation in Bovine Cortical Bone: An In Vitro Study, Ultrasound in Medicine & Biology
627 33 (12) (2007) 1933–1942. doi:10.1016/j.ultrasmedbio.2007.05.022.
628 URL <https://www.sciencedirect.com/science/article/pii/S0301562907002724>